

Neutron-neutron angular correlations in spontaneous fission of ^{252}Cf and ^{240}Pu J. M. Verbeke,¹ L. F. Nakae,¹ and R. Vogt^{1,2}¹*Nuclear and Chemical Sciences Division, Lawrence Livermore National Laboratory, P.O. Box 808, Livermore, California 94551, USA*²*Department of Physics, University of California, Davis, One Shields Avenue, Davis, California 95616, USA*

(Received 23 May 2017; published 2 April 2018)

Background: Angular anisotropy has been observed between prompt neutrons emitted during the fission process. Such an anisotropy arises because the emitted neutrons are boosted along the direction of the parent fragment.

Purpose: To measure the neutron-neutron angular correlations from the spontaneous fission of ^{252}Cf and ^{240}Pu oxide samples using a liquid scintillator array capable of pulse-shape discrimination. To compare these correlations to simulations combining the Monte Carlo radiation transport code MCNPX with the fission event generator FREYA.

Method: Two different analysis methods were used to study the neutron-neutron correlations with varying energy thresholds. The first is based on setting a light output threshold while the second imposes a time-of-flight cutoff. The second method has the advantage of being truly detector independent.

Results: The neutron-neutron correlation modeled by FREYA depends strongly on the sharing of the excitation energy between the two fragments. The measured asymmetry enabled us to adjust the FREYA parameter x in ^{240}Pu , which controls the energy partition between the fragments and is so far inaccessible in other measurements. The ^{240}Pu data in this analysis was the first available to quantify the energy partition for this isotope. The agreement between data and simulation is overall very good for $^{252}\text{Cf}(\text{sf})$ and $^{240}\text{Pu}(\text{sf})$.

Conclusions: The asymmetry in the measured neutron-neutron angular distributions can be predicted by FREYA. The shape of the correlation function depends on how the excitation energy is partitioned between the two fission fragments. Experimental data suggest that the lighter fragment is disproportionately excited.

DOI: [10.1103/PhysRevC.97.044601](https://doi.org/10.1103/PhysRevC.97.044601)

I. INTRODUCTION

Spontaneous fission is characterized by the emission of bursts of neutrons. These bursts are in turn amplified by the surrounding multiplying fissile materials to form fission chains. This unique fission chain signature has been used for many decades to detect and authenticate nuclear materials. Typically ^3He tubes record the arrival times of neutrons from fissile sources. Unfortunately the cross section for neutron capture in ^3He is only large enough for neutrons that have been thermalized in a moderating material. Scintillators, on the other hand, can directly detect unmoderated fission neutrons because inelastic scattering of neutrons on hydrogen results in the emission of a recoil proton, ionizing the scintillator material, enabling detection on a nanosecond timescale.

Because scintillators measure unmoderated prompt emission of neutrons from spontaneous fission, detection of nuclear materials such as plutonium becomes possible by measurements of the angular anisotropy between two neutrons. Almost all of the neutron emission in spontaneous and low-energy fission comes from the fully accelerated fission fragments whose back-to-back motion is imprinted on the neutron directions in the laboratory frame. Thus, small-angle correlations are expected from neutrons emitted from the same fragment, whereas large-angle correlations arise from opposite fragments. ^{240}Pu is a key isotope of plutonium because of its high spontaneous fission rate. In addition, its low-average neutron multiplicity suggests that it should exhibit a rather strong angular anisotropy. Thus, such measurements in $^{240}\text{Pu}(\text{sf})$ could

provide valuable information for identifying the composition of materials.

Neutron-neutron angular correlations have been measured in the past for $^{252}\text{Cf}(\text{sf})$ [1–5], $^{240}\text{Pu}(\text{sf})$ [6], and $^{235}\text{U}(n_{\text{th}},\text{f})$ [7]. These measurements were previously employed to search for evidence of scission neutrons, emitted from the nucleus prior to fission. These neutrons would be emitted isotropically in the laboratory frame. Discrepancies in the measured n - n angular correlations relative to simulations could be due to scission neutrons. No evidence was seen for an isotropic neutron source in Ref. [8]. However, those simulations using the FREYA code, also employed here, were not coupled to a model of the detector system via a neutron transport code and were thus not a comprehensive comparison. We can thus improve on the analysis in Ref. [8] with a full simulation of our detector. In addition, as was also shown in Ref. [8], the neutron-neutron angular correlation is most sensitive to the excitation energy sharing between the two fragments. Currently this sharing is modeled in FREYA by a single-valued parameter x . For $^{252}\text{Cf}(\text{sf})$, x was fixed by comparing to the neutron multiplicity as a function of the fragment mass. No such measurement is available to fix x for $^{240}\text{Pu}(\text{sf})$. Thus, a comparison between the n - n correlations measured here for this isotope with FREYA simulations could fix the x parameter for this case, as we discuss later.

In most measurements, the method for constructing correlations is based on setting different thresholds on the scintillation light output, leading to an energy-dependent set of correlations. Unfortunately, this method is detector-dependent, because

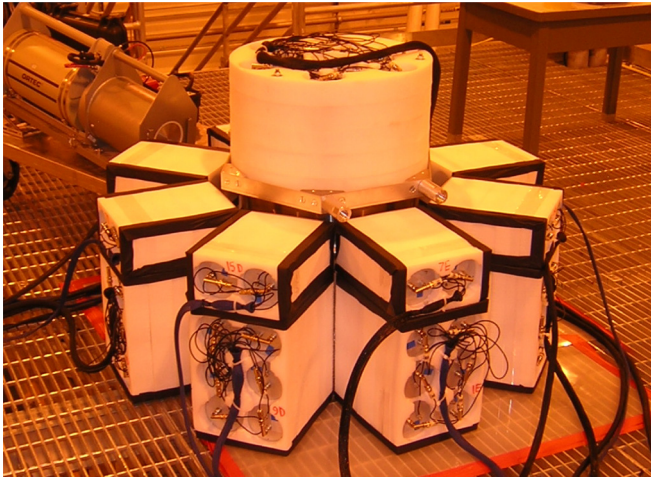


FIG. 1. Photograph of the 77 liquid scintillator array on low mass floor.

the detector materials, sizes, and data acquisition systems affect these measurements. For example, in large detectors, neutrons will produce more scintillation light by scattering and transferring energy to multiple proton recoils than in a smaller detector.

In this paper we propose a new method, based on neutron time-of-flight, to construct the kinetic energy of the measured neutron rather than relying on the recoil proton. To form correlations, we select neutrons with kinetic energies above a threshold, resulting in a truly detector independent correlation measurement.

The paper is organized as follows. We first describe the detector setup, discussing two methods to determine the dependence of the scintillator light yield function on proton recoil energy. We then describe the method used in Refs. [4–6] for determining correlations based on detector energy thresholds, including some of its shortcomings. Subsequently, we introduce an analysis based on the neutron time-of-flight to determine a detector-independent correlation function. Next, we introduce the fission model FREYA and describe how the measured correlations are simulated by incorporating FREYA into neutron transport codes. Our results are then compared to previous $^{252}\text{Cf}(\text{sf})$ and $^{240}\text{Pu}(\text{sf})$ data using the same energy thresholds to validate our method. The dependence of the results on detector size is also discussed. Next, we describe how we employ our simulations to eliminate detector cross talk. Finally, we compare Monte Carlo simulations using MCNPX with FREYA to the experimental data and describe how the neutron-neutron correlations could be used to determine the FREYA parameter governing the excitation energy sharing between the fragments when no other data exists. Finally we draw our conclusions.

II. DETECTOR SETUP AND EXPERIMENTAL METHOD

Figure 1 shows the geometrical configuration of the detector array used to measure the neutron-neutron correlations. The array consists of 77 scintillator detectors. Each detector in the array is cylindrical in shape, 10.16 cm diameter by 7.62 cm

deep, and filled with EJ-301 scintillating material [9]. Thirteen detectors sit over a cavity formed by an octagonal array underneath. Each arm of the octagon is a vertical tower made of eight scintillators. The measurement cavity is also octagonal, with 60 cm between the faces of opposite towers, and stands 50 cm tall. The tightly packed system has 2π solid angle coverage, resulting in an overall geometric efficiency of 50%.

Each of the 77 scintillators is individually read out by a photomultiplier tube. Data is acquired using a VME-based pulse digitizer for pulse-shape discrimination (PSD) and list mode data acquisition. The counter uses Struck SIS3316 fast ADC digitizers with a 160 MHz sampling rate and a 12-bit dynamic range. The digitizers have an input voltage range of ± 1 V. The digitizers allow subnanosecond timing of time-stamped physics events and allow the streaming of processed and compressed PSD information to reduce the overall data burden. The detector was originally designed for fast multiplicity counting and assaying of fissile material because the few nanosecond decay time of the scintillator material allows faster count rates than ^3He well counters.

A. Energy calibration

The energy calibration of the liquid scintillators was performed using a ^{137}Cs source placed in the middle of the detector array. Each γ interaction in the scintillator produces scintillation light, which is recorded by the photomultiplier tube (PMT) as an electric pulse. The pulse is digitized by an analog to digital converter (ADC) and the integral of the counts under the pulse is I_{ADC} . In a well calibrated detector, a photon of energy E_γ (keV) depositing all its energy in the scintillator produces a value of I_{ADC} which can be mapped back to E_γ . However, in a large array of detectors, the PMTs, scintillators, photocathodes, digitizers are not identical, and the integrals I_{ADC} will vary from detector to detector, for identical photon energy deposition. The mapping between I_{ADC} and E_γ is thus not unique across all detectors. To account for these differences, we use detector response functions $\text{DRF}(I_{\text{ADC}})$ to convert the integral I_{ADC} into a scintillation light output LO which has units of keVee. With these detector-dependent functions, photons with identical energies map onto the same LO, independently of the detector. The detector response functions have the following form:

$$\text{DRF}_\gamma(I_{\text{ADC}}) = a I_{\text{ADC}}(E_\gamma) \quad [\text{keVee}], \quad (1)$$

where the coefficient a depends on the scintillator/PMT assembly and is in units of keVee/(integral of ADC counts). The value of a is chosen so that, for a photon of energy E_γ transferring all its energy to electrons to eventually produce light, the value of the light output LO is equal to E_γ . These response functions are used to reconstruct the photon spectrum from the integrals I_{ADC} recorded by the PMT pulse digitizer. In Ref. [10] the detector response functions were shown to be linear in E_γ within 1%. Figure 2 shows the measured ^{137}Cs scintillation light spectrum for all 77 scintillators. The Compton edge for ^{137}Cs , at 477 keV, was detected by an algorithm described in Ref. [11] and was employed to set the values of the coefficients a for each individual detector.

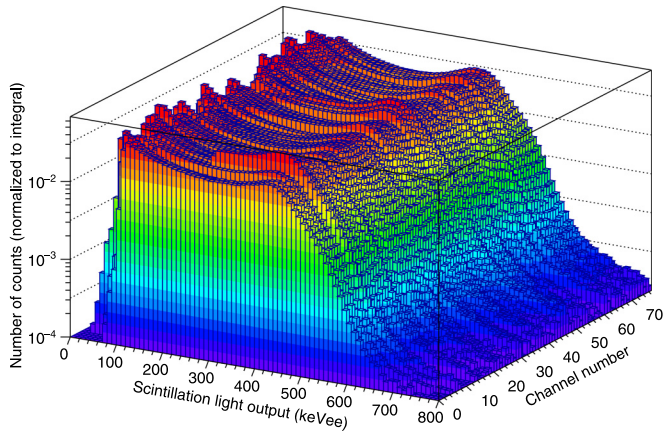


FIG. 2. Energy calibration of the 77 liquid scintillators using a ^{137}Cs source. The energy spectra is given for each channel number.

B. Pulse-shape discrimination

Neutron-photon pulse separation was achieved by simultaneous measurement of the charge in the PMT current, in the peak of the pulse, and the charge in the tail of the pulse, the so-called slow component. The method of pulse-shape discrimination (PSD) is described in Ref. [12].

Figure 3 shows neutron scores computed by the PSD algorithm for different detection events as a function of the electron-equivalent energy deposited by the event. The neutron score for digitized pulses is the ratio of the area under the tail to the area under the peak of the pulse. We can clearly distinguish two bands: the upper one, filled with neutrons, and the lower one, with photons. The magenta (light gray) outline in this plot defines a region where events are most likely neutrons and will be tagged as such by the data acquisition system. The black outline defines a region where events are tagged as photons. The two outlines can be referred to as neutron and photon acceptance regions from a PSD classifier perspective, and extend down to 100 keVee, below which PSD

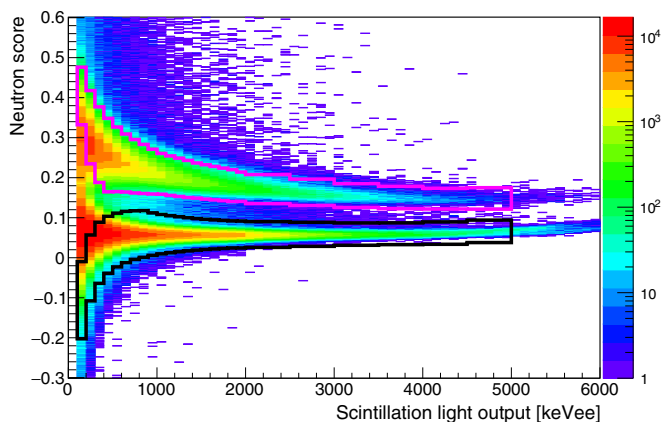


FIG. 3. Pulse-shape discrimination for one of the liquid scintillators. The regions of neutron (magenta or light gray outline) and photon (black outline) identification are shown. From a PSD classifier perspective, they can be referred to as the neutron and photon acceptance regions.

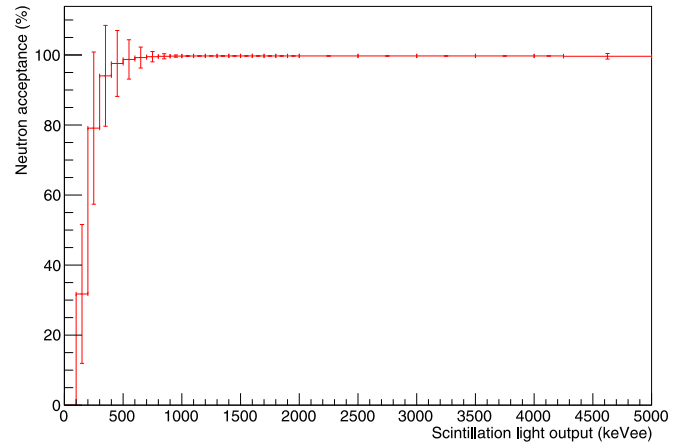


FIG. 4. Acceptance of neutron pulses as a function of scintillation light output and averaged over all detector channels. Bars indicate the dispersions around the means, from channel-to-channel variations.

was not attempted. The PMT biases were optimized to get good PSD for high-energy neutrons because our focus was not on the lowest energy neutrons. For electron-equivalent energies greater than 1 MeVee, the two bands do not overlap significantly, leading to good neutron-photon discrimination. Below 1 MeVee, discrimination slowly worsens and it becomes more difficult to distinguish neutrons from photons. In that energy region, photons encroaching on the neutron band push the outline of the positive neutron identification region upwards and lead to a number of neutrons that cannot be identified as such using the PSD classification algorithm. Shown in Fig. 4, the acceptance of neutron pulses degrades rapidly from 94% at 300 keVee down to 80% at 200 keVee and 30% at 100 keVee. At these low light outputs, the reduced acceptances not only depends on the PSD classifier but also on the reduced detector sensitivities to neutrons (see Figs. 2 and 7). Thus, there is significant degradation in neutron acceptance below 300 keVee. Our data was corrected for these neutron acceptances by adjusting the contributions of the n - n coincidences.

The ^{252}Cf source used for calibration emitted so few neutrons above 5 MeVee that it was difficult to define regions of positive neutron identification with great confidence above that energy. Because only 0.3% of the neutrons from ^{252}Cf (sf) have enough kinetic energy to produce proton recoils that can generate 5 MeVee of light output, this upper cutoff was deemed appropriate for these measurements. Events lying outside of these two bands, with equivalent energies of less than 100 keVee and greater than 5 MeVee, are treated as particles of unknown type. The region of positive photon identification slowly curves up above 5 MeVee. This effect is attributed to saturation effects in the electronics. Indeed, large enough pulses run into the dynamic range limit of the digitizers. This causes either the PMTs to saturate or the tops of the digitized pulses to be flattened or chopped off and the corresponding charge does not get integrated. For these high energies, the detector response loses its linearity. This is not critical for our experiment because we only consider electron-equivalent energies below 5 MeVee. One of the 77 scintillators was not

properly connected and acted erratically. It was turned off for the data analysis.

The neutron misidentification rate for this array of liquid scintillators was computed in Ref. [13]. The number of events misidentified as neutrons decreases with equivalent energy: it is on the order of 20 ± 4 ppm for a 100 keVee energy threshold; 13 ± 4 ppm for 200 keVee; 11 ± 3 ppm for 300 keVee; 9 ± 3 ppm for 400 keVee; and 7 ± 3 ppm for 500 keVee. The number of events misidentified as photons was not estimated because it is of limited relevance for this analysis.

C. Synchronization between detectors

It is essential that the liquid scintillators be synchronized with each other to accurately measure time intervals between detections in different detectors. Because neutron kinetic energies are computed from time-of-flight, the resolution of the time intervals has a direct impact on the resolution of the neutron kinetic energy. The liquid scintillators were synchronized using Compton scattering between detectors. The method use to synchronize the scintillators is described in Ref. [14]. We use the same ^{137}Cs data used for the energy calibration to synchronize the time interval between detectors. Photons emitted from ^{137}Cs will occasionally Compton scatter in one detector and register a second count in an adjacent detector, resulting in a time interval between detection equal to the photon time-of-flight between the two count locations. If the chronological order of the counts is reversed, the time interval between the counts will have the same amplitude but will be negative. The centers of adjacent detectors are approximately 10 cm apart, corresponding to a photon time-of-flight of 330 ps center-to-center. For infinite time resolution, we could thus expect two broad peaks ~ 330 ps apart with long tails on both sides because photons will Compton scatter in different locations within the detectors. The time interval distribution between counts is shown in Fig. 5 for our detector setup.

Because adjacent detectors are both large and close together, the two peaks are indistinguishable and have merged into a single peak. Fitting this peak with a Gaussian distribution, the standard deviation is 650 ps. Accounting for the photon time-of-flight, one can estimate the time resolution to be close to 500 ps.

D. Light output function

The emitted neutrons generate charged particles in the scintillator (mainly recoil protons) which produce light pulses. In addition, γ radiation creates photo or Compton electrons. However, protons and electrons of the same energy give light pulses of different amplitudes. Because the detector energy calibration is carried out with photon sources, the relation between proton and electron energies is determined employing the light output function.

The light output scale is defined in terms of the equivalent electron energy LO, which is the light output for an electron depositing the corresponding energy inside the scintillator; i.e., a proton of the energy E_p gives the same light output LO as an electron of the equivalent energy LO.

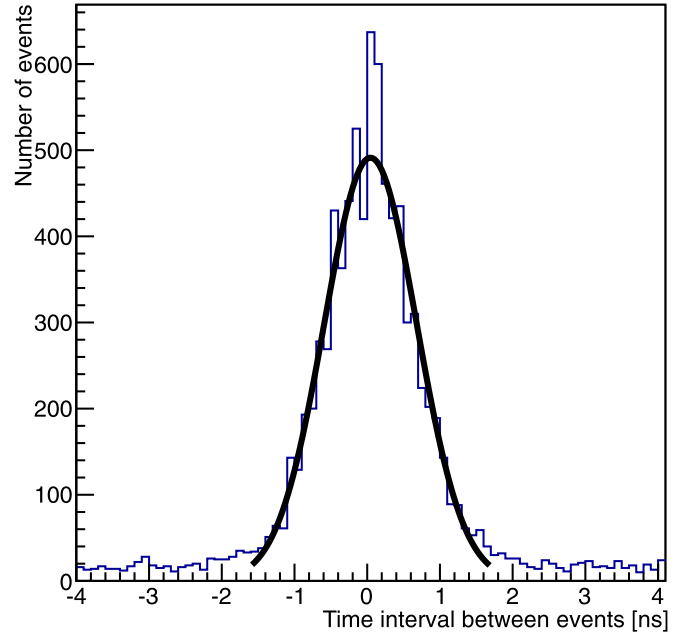


FIG. 5. Distribution of time intervals between counts in adjacent detectors.

Cecil's exponential model [15] is chosen as the functional form of $\text{LO}(E_p)$,

$$\text{LO}(E_p) = aE_p - b[1 - \exp(-cE_p^d)] \quad [\text{keVee}]. \quad (2)$$

The coefficients a , b , and c were determined by fitting time-of-flight spectra with different light output thresholds. For a given scintillation light output LO, Eq. (2) can be used to determine the recoil proton energy E_p necessary to produce the same amount of light as an electron of energy LO keVee would.

Figure 6 shows the time-of-flight distributions using 16 detectors at the same distance from the $^{252}\text{Cf}(\text{sf})$ source and setting a 100 keVee threshold on the light output. The blue (top)

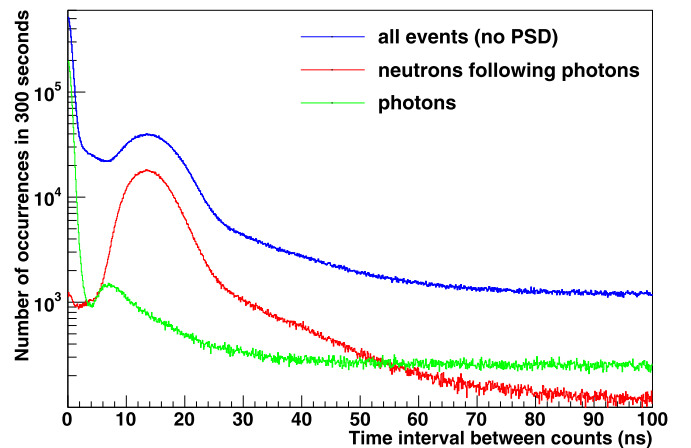


FIG. 6. Distribution of time intervals between counts for the $^{252}\text{Cf}(\text{sf})$ source measured with a subset of the liquid scintillator array. A light output threshold of 100 keVee is applied.

curve shows the distribution of time intervals between any two detections in the array before PSD is applied to distinguish neutrons from photons. Thus, this distribution also includes all the events outside of the black and magenta (light gray) outlines in Fig. 3, explaining its larger magnitude. The green (bottom curve at 15 ns) curve is the distribution of time intervals between photon detections, and the red (middle curve at 15 ns) curve is the time interval for a photon detection followed by a neutron. The maximum proton recoil energy can be determined from a precise measurement of the time difference between the signals and particle identification through the observed signal shape. The maximum proton recoil energy for a given scintillation light output threshold is determined from fitting the red (middle curve at 15 ns) curve in Fig. 6 while accounting for the background. This method, described in Ref. [16], enabled us to determine the coefficients of Cecil's exponential model in Eq. (2).

As an alternative to this conventional time-of-flight approach, we can use the measured scintillation light pulse height distribution (PHD) to determine the light output as a function of the proton recoil energy [17,18]. Indeed, employing the MCNPX 2.7.0 Monte Carlo code, we can accurately model sources and detectors and simulate the collision of each source neutron with hydrogen atoms in each individual detector. To construct the scintillation light produced by the simulated proton recoils from a source neutron, we apply Cecil's law to the proton recoil energies and sum up the light to form an individual light pulse. This method is repeated for all source neutrons to obtain a scintillation light PHD.

Our constructed scintillation light PHD can be compared to the measured one to fix the parameters of the exponential expression for the light output and thus reconstruct the measured PHD. We note that if we assume that neutrons only collide once per detector, it would be straightforward to construct the proton recoil PHD by considering the contributions of each source neutron to this distribution and converting it to a scintillation light PHD using the exponential form. However, due to the nonlinearity of the light output function, the single scattering assumption is only valid if the neutrons generate one single proton recoil per detector, i.e., for small detectors.

The optimization yielded the parameters $a = 0.81$, $b = 6.3$, $c = 0.09$, and $d = 1$ in Eq. (2). The results in terms of PHD are shown in Fig. 7.

In the range 200 keV to 3.5 MeV, the differences between simulated and experimental PHD vary from 0 to 18% with an average of 5%. Except for small discrepancies likely due to insufficient model details in the simulation, the simulated PHD, shown in Fig. 7, is consistent with the one measured experimentally. The jagged structure at low light outputs comes from neutron rejection by the neutron identification algorithm (see Fig. 3). This results in reduced detector efficiencies for low neutron energies. The detection sensitivity to epithermal neutrons, which varies from detector to detector, is reduced as well because the high-voltage biases on the photomultiplier tubes require a minimum light pulse height close to 100 keVee. Also note that the measured pulse height spectrum is truncated at 5 MeVee because PSD is no longer reliable above that energy in our configuration.

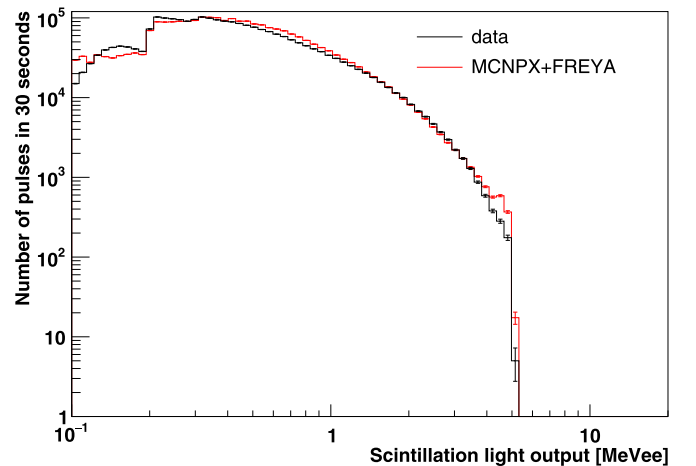


FIG. 7. Measured (black) and simulated (red or light gray) pulse height distributions produced by a $^{252}\text{Cf}(\text{sf})$ source recorded by the scintillators.

E. Neutron detection efficiency

The overall neutron detection efficiency of the scintillators is 7.8%. In Table I, the average neutron detection efficiency is given as a function of the threshold applied to the scintillation light output. A light output threshold is dialed to filter out neutrons with low light output and to compute a LO-dependent neutron detection efficiency.

As an alternative, the detection efficiency can be determined as a function of the neutron kinetic energy using Eqs. (4) and (5) of the time-of-flight approach described in Sec. III B. In this case, the neutron detection efficiency can be inferred from the strength and spectral properties of the spontaneous fission source. Figure 8 shows the average neutron detection efficiency of the scintillators for neutrons of kinetic energies varying from 400 keV to 10 MeV. This plot is important as it shows the sensitivity of the detectors to neutrons of various kinetic energies, and in particular to neutrons emitted by $^{252}\text{Cf}(\text{sf})$ and $^{240}\text{Pu}(\text{sf})$. The detector efficiency peaks at 2.6 MeV. For neutrons with kinetic energy lower than 2 MeV, the efficiency drops with decreasing energy because fewer

TABLE I. Average neutron detection efficiency of the scintillators as a function of the scintillation light output threshold LO.

LO (MeVee)	Efficiency (%)
0.1	7.8
0.2	6.7
0.3	4.8
0.4	3.5
0.5	2.5
0.6	1.9
0.7	1.5
0.8	1.2
0.9	0.95
1.0	0.75
1.5	0.29
2.0	0.12

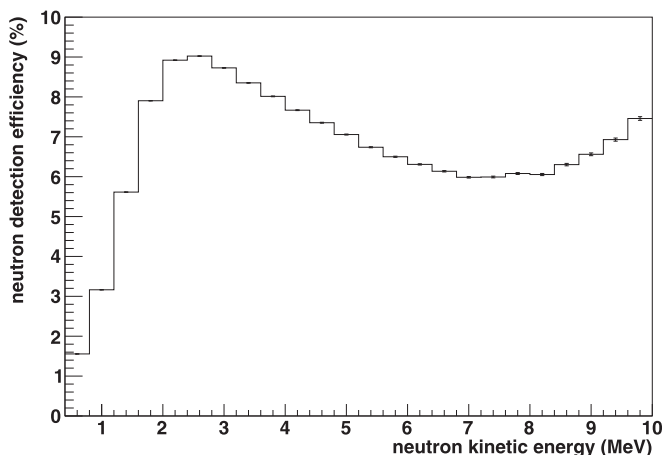


FIG. 8. Average neutron detection efficiency as a function of kinetic energy, for a scintillation light output threshold of 100 keVee.

and fewer proton recoils yield enough scintillation light to be within the bounds of the neutron acceptance region shown in Fig. 3. For kinetic energies greater than 8 MeV, the efficiency increases artificially. To understand this increase, see the curve labeled “neutrons following photons” in Fig. 6. This contribution should vanish for time intervals smaller than ~ 5 ns because the only neutrons that can travel to the detectors in less than 4.5 ns are neutrons with energies greater than 20 MeV. Instead of vanishing, there are a finite number of events in this region. These events can be attributed to high energy neutrons that inelastically scatter off the detector and surrounding materials. Inelastic scattering reactions generate secondary photons. These photons are delayed by the travel time of the spontaneous fission neutrons to the detectors and are detected on a timescale comparable to that of neutrons originating from the same spontaneous fission. The quasicoincidences of these photon-neutron pairs fill the region of short time intervals in Fig. 6. In addition, the neutrons in these photon-neutron pairs are erroneously tagged as high energy neutrons, resulting in the artificial increase in neutron efficiency for neutrons with kinetic energies greater than 8 MeV in Fig. 8. Fortunately, the fraction of misidentified high energy neutrons is $< 2\%$.

The detector efficiencies are implicitly taken into account in the simulations by using the neutron energy-dependent cross sections from the data libraries.

III. ANALYSIS METHOD

Two different methods are presented to measure the angular correlations between fission neutrons. The first, using detector thresholds as a neutron filter, has been rather widely used in these analyses. Thus, even though it has some shortcomings, as we discuss, we will use it to compare our measurements to previous data. The other, using neutron time of flight to filter neutrons, resulting in a detector independent analysis, is introduced here for the first time. Since it is a new approach, we only show results using this method at the end of this paper, after comparison to previous data and simulations.

A. Detector thresholds as a neutron filter

The first method uses the detection threshold of the scintillators to filter low-energy neutrons. This method was used in Gagarski [4] and Pozzi [5] to measure the angular distribution of correlated spontaneous fission neutrons emitted by ^{252}Cf , and by Marcat [6] for ^{240}Pu . To validate our experimental measurements and methodology, we will compare our data to their results.

Two neutrons are assumed to arise from the same spontaneous fission if they are detected within 40 ns of each other. These neutrons are correlated. Two detected neutrons are uncorrelated if the second neutron is at least $100 \mu\text{s}$ away in time from the first neutron. A time window opens $100 \mu\text{s}$ after the first neutron to count uncorrelated neutrons. The duration of this time window depends on the neutron source strength. It is 1 ms for our $^{252}\text{Cf}(\text{sf})$ source and 100 ms for the weaker $^{240}\text{Pu}(\text{sf})$ source. The ratio of correlated to uncorrelated event rates is proportional to the probability of detecting two spontaneous fission neutrons in some angular bin.

While the angular distributions produced by this method are useful, there are some disadvantages that we now discuss.

Although the neutron energy deposition in a scintillator is proportional to the kinetic energy of the incident neutron, it also depends on its scattering angle via elastic scattering. Some high-energy neutrons might scatter on hydrogen with a grazing angle, not depositing enough energy to register a count, whereas some lower-energy neutrons could register a count with a head-on collision on hydrogen. As a result, the neutron detection threshold imposed on the scintillators does not map onto a single incident neutron kinetic energy threshold.

The probability for the resulting light yield to be above the threshold is a function of the detector volume. For a given threshold, the population of incident neutrons counted in a small detector will be of considerably higher energy than the population in a larger one. Indeed, the number of times a neutron scatters in a volume is a function of the detector volume. In a small detector, a neutron of a given energy will scatter fewer times than in a larger detector, transferring thus less energy to recoil protons.

The selected energy threshold is measured along a scale graduated against γ rays. To find out the equivalent neutron kinetic energy, it is necessary to determine the light output function. A survey of the literature [17, 19, 20] indicates that the neutron light output depends on the scintillating material, detector geometry, hardware settings, etc. Measuring it requires a separate, dedicated experiment.

B. Time-of-flight as a neutron filter

Instead of using a detection threshold to filter low-energy neutrons, we propose to use time-of-flight as an alternate approach. Here a photon from spontaneous fission is used to open a time-of-flight measurement window and a neutron is employed to close it.

We assume a spontaneous fission source, located at $(x_{\text{src}}, y_{\text{src}}, z_{\text{src}})$, emits neutrons and photons. One of the photons is detected in a scintillator. This first detection serves as a trigger. Employing this trigger and the distance from the detector to the source, it is possible to determine how much time

TABLE II. Time interval Δt for a given neutron kinetic energy determined by neutron time-of-flight method. Uncertainty ΔE_{kin} on neutron kinetic energy E_{kin} given the finite detector time resolution of 500 ps. A source to detector distance of 30 cm is assumed.

E_{kin} (MeV)	Δt (ns)	ΔE_{kin} (keV)
0.5	29.67	16
1	20.68	48
2	14.34	136
3	11.52	256
4	9.844	396
5	8.700	558

has passed since the spontaneous fission occurred. Next, one of the spontaneous fission neutrons is detected. The time-of-flight of that spontaneous fission neutron is the time elapsed from the spontaneous fission to the neutron detection. The time interval between the γ -ray detection at $(x_\gamma, y_\gamma, z_\gamma)$ and the neutron detection at (x_n, y_n, z_n) is

$$\Delta t = \frac{1}{v_n} \sqrt{(x_{\text{src}} - x_n)^2 + (y_{\text{src}} - y_n)^2 + (z_{\text{src}} - z_n)^2} - \frac{1}{c} \sqrt{(x_{\text{src}} - x_\gamma)^2 + (y_{\text{src}} - y_\gamma)^2 + (z_{\text{src}} - z_\gamma)^2}, \quad (3)$$

where c is the velocity of the photon (the speed of light) and v_n is the velocity of the neutron. The expression above for the time interval can be used to determine the velocity v_n ,

$$v_n = \frac{\sqrt{(x_{\text{src}} - x_n)^2 + (y_{\text{src}} - y_n)^2 + (z_{\text{src}} - z_n)^2}}{\Delta t + \frac{1}{c} \sqrt{(x_{\text{src}} - x_\gamma)^2 + (y_{\text{src}} - y_\gamma)^2 + (z_{\text{src}} - z_\gamma)^2}}. \quad (4)$$

Once v_n is determined, the neutron kinetic energy can be calculated as

$$E_{\text{kin}} = \frac{1}{2} m_n v_n^2. \quad (5)$$

Inversely, the measured time interval Δt can be calculated as a function of the neutron kinetic energy. Several values of Δt are listed in Table II for some representative neutron kinetic energies.

Assuming a threshold $E_{\text{kin}}^{\text{thr}}$ for the neutron kinetic energy, Eqs. (3)–(5), makes it possible to filter all neutrons with $E_{\text{kin}} < E_{\text{kin}}^{\text{thr}}$.

For all neutrons with $E_{\text{kin}} \geq E_{\text{kin}}^{\text{thr}}$, two neutron detections are assumed to stem from the same spontaneous fission if both occur within a time interval $\Delta t + \text{TOF}_\gamma$. (Recall that this time interval depends on the threshold $E_{\text{kin}}^{\text{thr}}$, as shown in Table II where TOF_γ is the photon time-of-flight.) Two such neutrons are likely correlated with the spontaneous fission unless the two counts arise from the same neutron (neutron cross talk), which is discussed later.

As in the case for using detection thresholds as a filter, the ratio of correlated to uncorrelated event rates is proportional to the probability of detecting two spontaneous fission neutrons in some angular bin.

We can also determine the uncertainties on the neutron kinetic energy given the finite time resolution of the detector using Eqs. (3)–(5). We assume that the distance between the source and the detectors is uniformly 30 cm. For neutrons

of kinetic energy 500 keV, the 500 ps resolution leads to an uncertainty of 16 keV on the neutron kinetic energy. Table II lists the uncertainties on the neutron kinetic energies given the 500 ps resolution of the scintillators.

A larger uncertainty on the neutron kinetic energy arises from the depth of the detectors. Indeed, neutrons can scatter anywhere in the detector volume, resulting in an uncertainty of approximately 7.62 cm on its travel distance or a variance $\sigma^2 = (2.2 \text{ cm})^2$ in the numerator of Eq. (4) assuming a rectangular function for the location of interaction within the source. This variance translates into a relative standard deviation of 13% on the kinetic energy of the neutron.

Now the neutron kinetic energies are calculated based on time-of-flight and not on the energy deposited in the scintillators. They are thus independent of the neutron kinematics in the scintillators. We note that, with the PMT voltage setting used in the experiment, a neutron transferring less than 100 keVee to a recoil proton is unlikely to be detected. The population of these neutrons is reduced as the neutron kinetic energy threshold is raised. This method enables us to determine neutron-neutron angular distributions with different kinetic energy thresholds by filtering out incident neutrons based on kinetic energy rather than energy deposition. This method thus has the advantage of forming truly detector independent correlation measurements.

Another advantage of the time-of-flight approach to measure n - n angular correlations is that the type of particle associated with a detection can be determined using a combination of PSD and time-of-flight. Indeed, photons and neutrons can be discriminated based on their relative velocity. We will see in Sec. VII that the neutron detection efficiency can be substantially increased using both of these quantities for particle classification.

IV. SIMULATIONS

General-purpose Monte Carlo codes such as MCNP6 [21], TRIPOLI-4 [22,23], TART [24], and COG [25] are available for modeling neutron transport. They have traditionally employed “average fission models” for modeling fission, characterized by uncorrelated secondary particle emission, sampling from the same probability density functions. This approximation is sufficient for the calculation of average quantities such as flux, energy deposition and multiplication. However, correlations are important, for example, for modeling neutron multiplicity counters, because determinations of the multiplication and mass of unknown objects are based on measuring time-correlated neutrons.

To address these deficiencies, analog fission physics was added to Monte Carlo codes over the years. MCNP-DSP [26] was the first code to include full neutron multiplicity distributions from fission. MCNPX-PoliMi [27,28] followed suit and included full neutron and γ -ray multiplicity distributions from fission. Later, the LLNL Fission Library [29], integrated into MCNPX2.7 [30] and Geant 4.9 [31], featured time-correlated sampling of neutrons and photons from neutron-induced fission, photofission, and spontaneous fission. Several of these codes have been used and validated for multiplicity counting systems [32–34]. The correlation capabilities for these codes are, however, limited as they sample outgoing

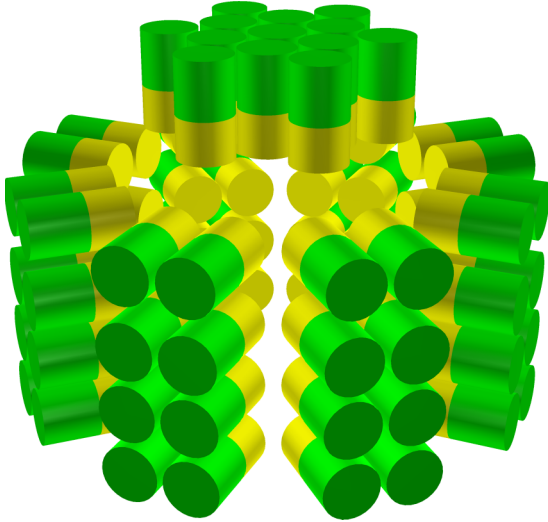


FIG. 9. MCNPX 2.7.0 model of the liquid scintillator array. Scintillators are in yellow (light gray), PMTs in green (dark gray).

particles from average fission distributions instead of sampling them from individual realizations of a fission process.

In recent years, various treatments have addressed fluctuations of and correlations between fission observables. In particular, a Monte Carlo approach was developed for the sequential emission of neutrons and photons from individual fission fragments in binary fission [35,36]. The more recent event-by-event fission model, FREYA, has been specifically designed for producing large numbers of fission events in a fast simulation [8,37–42]. Employing nuclear data for fragment mass and kinetic energy distributions, using statistical evaporation models for neutron and photon emission, and conserving energy, momentum, and angular momentum throughout, FREYA is able to predict a host of correlation observables, including correlations in neutron multiplicity, energy, and angles, and the energy sharing between neutrons and photons. FREYA can currently handle neutron-induced fission of ^{233}U , ^{235}U , ^{238}U , ^{239}Pu , ^{241}Pu , as well as the spontaneous fission of ^{238}U , ^{238}Pu , ^{240}Pu , ^{242}Pu , ^{244}Cm , and ^{252}Cf .

The latest version of FREYA 2.0.2 [43], coupled to the LLNL Fission Library for ease of incorporation, can be called from transport codes. In particular, the LLNL Fission Library/FREYA 2.0.2 has been implemented in the latest release of MCNP 6.2. The combination of MCNP 6.2 and LLNL Fission Library/FREYA 2.0.2 enables users to directly model fission event-by-event and transport fission secondaries through complex detector geometries while keeping them fully correlated from generation to detection.

To simulate the experimental angular correlation, we used a simplified MCNPX 2.7.0 [30] model developed for the large array of liquid scintillators shown in Fig. 1. A number of elements were not included in this simplified model, shown in Fig. 9: the low mass floor; the room walls and ceiling, which were 5 m away; the low-density foam holding the liquid scintillators and PMTs; the detector walls; etc. Additional simulations showed that the inclusion of these details made no difference in our analysis. Using a customized [44] version of MCNPX 2.7.0 with the LLNL Fission Library/FREYA

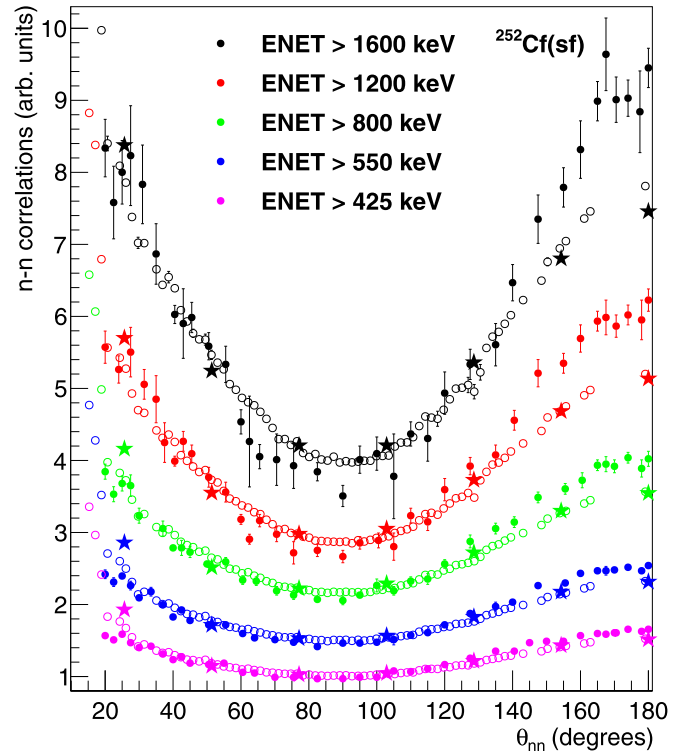


FIG. 10. Our two-neutron angular correlation for $^{252}\text{Cf}(\text{sf})$ as a function of the angular separation. The open circles are based on 30 minutes of data taking and were adjusted for neutron acceptance. The Gagarski [4] and Pozzi [5] results are shown by the filled circles and stars, respectively. From the top to the bottom curves: 1600, 1200, 800, 550, and 425 keV.

[29,43,45] turned on, we ran simulations to study neutron-neutron angular correlations.

V. COMPARISON TO PREVIOUS DATA USING DETECTOR THRESHOLDS

A. $^{252}\text{Cf}(\text{sf})$ measurements

The ^{252}Cf source used for our measurements was manufactured in 1997. Its initial intensity was 3.694×10^7 neutrons/s. The casing of the source has a small effect on the outgoing neutrons from fission. The source contains some contamination from ^{250}Cf . Because the half-life of ^{250}Cf is longer than that of ^{252}Cf , the fraction of fission neutrons originating from ^{250}Cf increases with time. Based on the initial composition and branching ratios for these sources, 1.9% neutrons originate from spontaneous fission of ^{250}Cf . The data analyzed here were collected by placing the $230 \mu\text{Ci}$ ^{252}Cf source in the center of the detection system for 30 minutes.

The open circles in Fig. 10 show our anisotropic angular distributions as a function of the angle between two spontaneous fission neutrons for different energy thresholds. The variance on the angle of correlation, governed by the size of the scintillators and the distance to the source, is $\sigma^2 = (5.8^\circ)^2$. The large number of data points in Fig. 10 arises because we have 76 active detectors, and thus 76×75 pairs of detectors with as many angular separations between detectors. Using

TABLE III. Number of neutron pairs counted for all detector pairs, for the ENET values 425, 550, 800, 1200, and 1600 keV, for ^{252}Cf .

ENET (keV)	Neutron pairs
425	18 320 600
550	16 446 500
800	12 499 500
1200	5 734 410
1600	2 594 990

a large array of detectors has a major advantage: one can measure the correlation function over a large range of angles with small separations in a single experiment. It is noteworthy that the experiment took only 30 min, whereas the Gagarski experiment described below with only two detectors took 50 days. Given the size of each detector and the PMT assembly, the smallest angular separation between detectors that could be achieved is 15° . The largest separation angle achievable, aside from diametrically opposed detectors that result in $\sim 180^\circ$, is approximately 165° .

Table III lists the number of correlated neutron pairs for all detector pairs as a function of ENET.

Data points from other experiments are more sparse because the detector arrays in these measurements employed fewer array elements. All data points include error bars. The Gagarski experiment had two identical stilbene crystals 40 mm diameter by 60 mm deep and shielded with borated polyethylene and lead to prevent cross talk. The angle between the two crystals as seen from the source was varied in steps of 5° – 10° in the interval 20° – 180° for a total of 36 different angles. The crystals were 40 to 70 cm from a ^{252}Cf source, the greater distance was necessary due to the dimensions of the detector shielding. The Pozzi *et al.* experiment employed 14 cylindrical EJ-309 scintillators of dimension 7.62 cm diameter by 5.08 cm deep. The detectors were on a circle and their locations fixed, the face of each detector was 20 cm from the source. Because the detectors were equally spaced, this configuration enabled the measurement of seven different angles in steps of 26° . The error bars are too small to show for the Pozzi data.

The data in the two reference experiments were not corrected for cross talk, so for comparison, our data in Fig. 10 is not either. Cross talk explains why Pozzi's data points at 26° are higher than the other data points. Indeed the detectors separated by 26° are neighbors and do not have a large distance nor material between them to minimize the number of neutrons scattering from one detector to the other.

By setting lower event selection boundaries with respect to the peak integral of PMT signals in the offline analysis, we obtained the experimental dependence of the neutron-neutron coincidence counts on the angle between the emitted neutrons for the equivalent neutron energy thresholds (ENET) published in Ref. [4]: 425, 550, 800, 1200, and 1600 keV. When ENET increases, fewer correlated neutrons are counted. This explains why the uncertainties on the data points increase for larger ENET values.

Some remarks about the ENETs are in order. For a 425 keV neutron to register a count above the 425 keV ENET, it

would take a single head-on collision with hydrogen. Any other scattering angle would result in the collision not being counted. Assuming neutrons could only scatter once per detector, this ENET would be equivalent to the energy transferred to the proton recoil and could thus be referred to as a proton recoil energy threshold. However, simulations show that most neutrons scatter multiple times within a single detector. Accounting for multiple collisions, the ENET could be reached by adding up the light output produced by the different proton recoils. (Note that the sum of the light output is a nonlinear function of the proton recoil energy.) Therefore, we refer to this threshold as the equivalent neutron energy threshold, and not as proton recoil energy threshold.

Previous measurements [1,3] indicate a quasisymmetric angular distribution. However, our data, shown in Fig. 10, has a distribution that peaks at angles close to 0° . This peak is the result of multiple scattering between detectors. Indeed, while neutrons are captured in ^3He tubes, they survive their scattering with protons in liquid scintillator cells and may be recorded a second or even a third time in neighboring detectors, even though this probability decreases as they lose energy [13].

Except for the region where neutron cross talk is important (angles close to 0°), the agreement between our measurements and the measurements of Gagarski [4] and Pozzi [5] is reasonable. The differences can be attributed to the sensitivity of the neutron-neutron correlations analyzed by this method to the detector material and geometry, a sensitivity which plagues this method of measuring neutron-neutron correlations. They could also be related to differences in detector sensitivities, which are shown here in Fig. 8 but are not given in Refs. [4,5]. The agreement of our data with the results of Refs. [4,5] validates our data taking and analysis.

We note that the data shown in Fig. 10 is the raw data, not accounting for cross talk between detectors. The correction for cross talk will be studied in Sec. VC.

B. Detector volume effects

In this section, we study the sensitivity of neutron-neutron correlations to detector volume. Because the detector volumes used in our analysis differs from those employed by Gagarski and Pozzi it is important to understand the sensitivity of the measurements to this effect. It would be equally important to assess their sensitivity to detector shielding, scintillation materials and other parameters, but this is beyond the scope of this work.

It is obvious that neutrons will scatter fewer times in smaller detectors than in larger ones. As a result, for a given equivalent neutron energy threshold, the population of neutrons counted in a smaller detector (à la Gagarski) will be, on average, higher energy than the population of detected neutrons in a larger detector. To study the effect of detector size, we halved the dimensions of the detectors (5.08 cm diameter by 3.81 cm deep, instead of the 10.16 cm diameter by 7.62 cm deep used in the experiment) in our Monte Carlo simulations. Figure 11 shows the ratio of the resulting neutron-neutron angular correlations, where we arbitrarily set the ratio to 1 for a separation angle of 90° . The graphs show saddles with local minima around 90° . Small ($\sim 35^\circ$) and large ($\sim 163^\circ$) separation angles lead

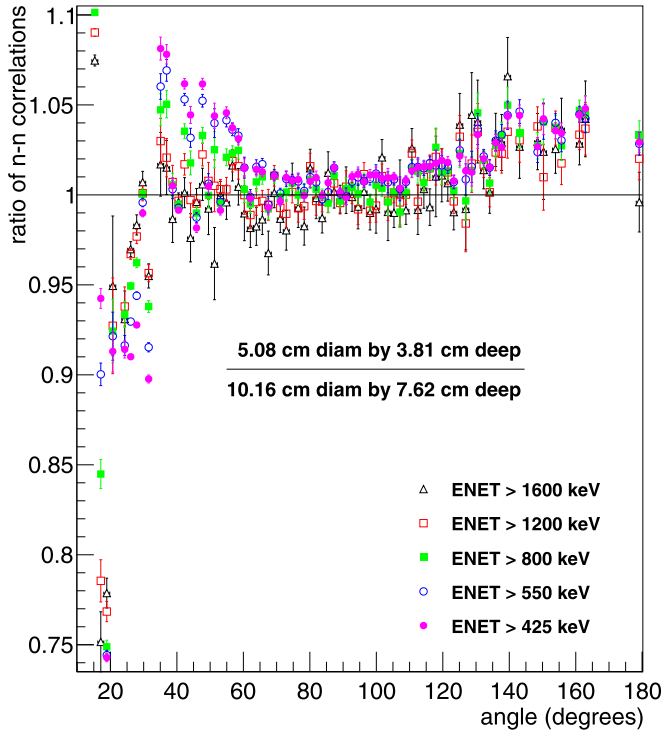


FIG. 11. The ratio of two-neutron angular correlations for $^{252}\text{Cf}(\text{sf})$ in a small detector relative to a large detector. Ratio arbitrarily set to 1 at 90° . The ratio shows the sensitivity of the correlations to the detector size based on FREYA simulations.

to neutron-neutron correlations 8% larger than at 90° . This increase follows from the higher average energy of the neutron population detected by smaller detectors. Indeed, neutrons will scatter fewer times within a small detector than within a larger one. The scintillation light produced will thus be lower. For a given scintillation light threshold, some neutrons that produce enough light to be detected in a large detector will be below the threshold in a small detector and therefore pass through undetected. For angular separation below 35° , neutron cross talk dominates and strongly depends on the distances between nearby detectors.

Figure 11 shows that the size of the detector has an effect on the neutron-neutron angular correlations. The distribution curvature will thus vary with detector size, making this method detector-sensitive. Because this method is sensitive to detector geometry, differences between the three results shown in Fig. 10, which all used different scintillator materials and different size detectors, can be expected.

C. $^{240}\text{Pu}(\text{sf})$ measurements and cross-talk correction

In this section, we describe our angular correlation measurement of $^{240}\text{Pu}(\text{sf})$, discuss our cross-talk correction, and compare our results with earlier data measured by Marcath *et al.* [6]. The measurements were carried out using a 4.5 g sample of ^{240}Pu (98% pure). Its initial intensity was 4,590 neutrons/s. Other plutonium isotopes accounted for less than 2% of the plutonium weight. The fraction of fission neutrons originating from these isotopes is negligible because of their

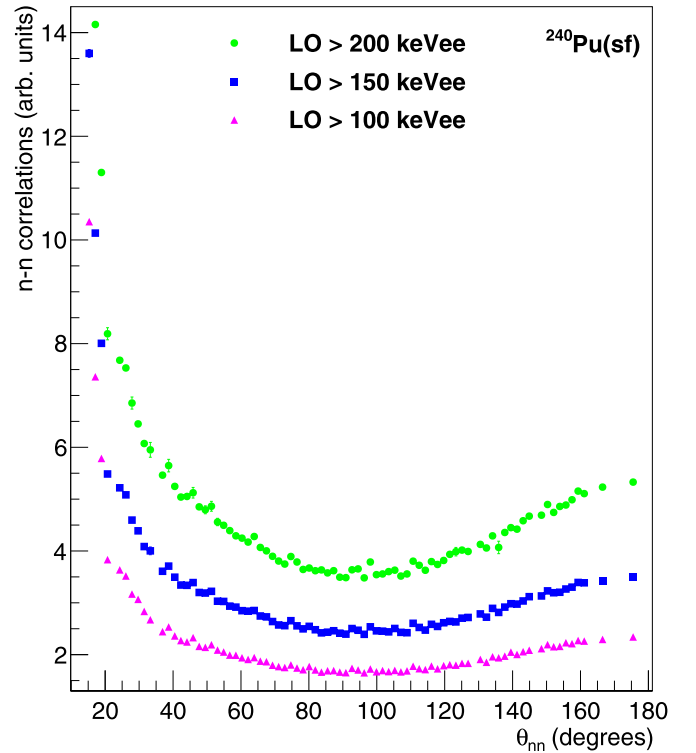


FIG. 12. The two-neutron angular correlation for $^{240}\text{Pu}(\text{sf})$ as a function of the angular separation before cross-talk correction and for several light output thresholds. The data points are based on 23 h of data taking and were adjusted for neutron acceptance.

relatively low spontaneous fission yields. Because the sample is oxidized, $\sim 14\%$ of the neutrons emitted are from (α, n) reactions. However, these neutrons are emitted individually and thus do not generate correlations, except for contributions due to neutron cross talk, which has been removed via the correction method described here. The data analyzed here were collected by placing the ^{240}Pu source in the center of the detection system for 23 h.

The thresholds used in this analysis are not the equivalent neutron energy thresholds required for our comparison to the Gagarski and Pozzi data but are, instead, electron equivalent energy thresholds E_γ to compare to the $^{240}\text{Pu}(\text{sf})$ measurements by Marcath [6]. We will use electron equivalent thresholds in the remainder of this section.

Figure 12 shows the raw two-neutron angular correlation for $^{240}\text{Pu}(\text{sf})$. No neutron cross-talk correction has yet been applied. There is a prominent peak at 0° . Table IV lists the number of correlated neutron pairs for all detector pairs as a function of the light output threshold LO.

We now discuss how we have tried to simulate and remove cross talk, essential for a comparison to the Marcath data. There is no reliable experimental analysis that could isolate counts due to cross talk on an event-by-event basis. However, simulations can be used to remove integral cross-talk counts from the experimental coincidences [6,46,47]. To study the effect of multiple scattering in our array, we modified the simulation so that, at most, one fission neutron is emitted per spontaneous fission $P(\nu) = 0$ for $\nu \geq 2$, suppressing

TABLE IV. Number of neutron pairs counted for all detector pairs, as a function of the light output threshold, for ^{240}Pu .

LO (keVee)	Neutron pairs
100	1 993 380
150	1 760 670
200	1 515 750
300	762 531
400	383 142
500	203 012

coincidences originating from the simultaneous emission of multiple spontaneous fission neutrons. The only coincidences in this case are due to individual neutrons registering multiple counts in adjacent detectors. It is possible for two neutrons emitted from two different spontaneous fissions to be counted in coincidence. However, even for our strong californium source, the probability for such events is ~ 0.01 accidental coincidences in a 30-min measurement interval.

For these simulations, we collect the rates of false coincidences due to neutron cross talk for each pair of detectors. These rates are compared to the rates when full multiplicity distributions are modeled for spontaneous fission. The ratio of the single neutron rates to the rates with the full $P(\nu)$ gives the fraction of coincidences that contaminate the true neutron correlations.

The simulated cross-talk contribution is shown in Fig. 13 as a function of the detector separation angle, as seen from the source. In the data, it is important to account for the scintillation light-dependent neutron detection efficiency of the detectors (see Sec. II B).

Because of the energy-dependent PSD rejection and detector sensitivity to neutrons, the efficiency for detecting neutrons tends to decrease for lower scintillation light output. Neutron cross talk at large angles is not as strong here as in the Marcath data [6], due to the presence of large masses of low- Z materials around each detector in the array which effectively shields them from each other. For angles smaller than 30° , however, the correction is large, 37% to 68%, depending on LO.

Figure 14 shows our results for $^{240}\text{Pu}(\text{sf})$ after correcting for cross talk. (Note the different scale on the y axis relative to Fig. 12.) We also now compare to the Marcath data. At small angles, less than 30° , the neutron-neutron correlation measurements appear to be slightly different from the Marcath data. This can be attributed to differences in detector sensitivities, shown here in Fig. 8 but not reported in Ref. [6], to inaccurate modeling of either the scintillation material or the scintillator geometry for the cross-talk correction, or to the sample position uncertainty which affects the simulated cross talk. At low detector angles, the cross-talk contribution is very sensitive to small changes in the sample position. It could also be attributed to an overprediction of the zero degree correlation in the FREYA simulation of the neutron cross talk. The overall good agreement between data sets is encouraging because our approach is completely independent, including different detectors, experimental setups, and analyses.

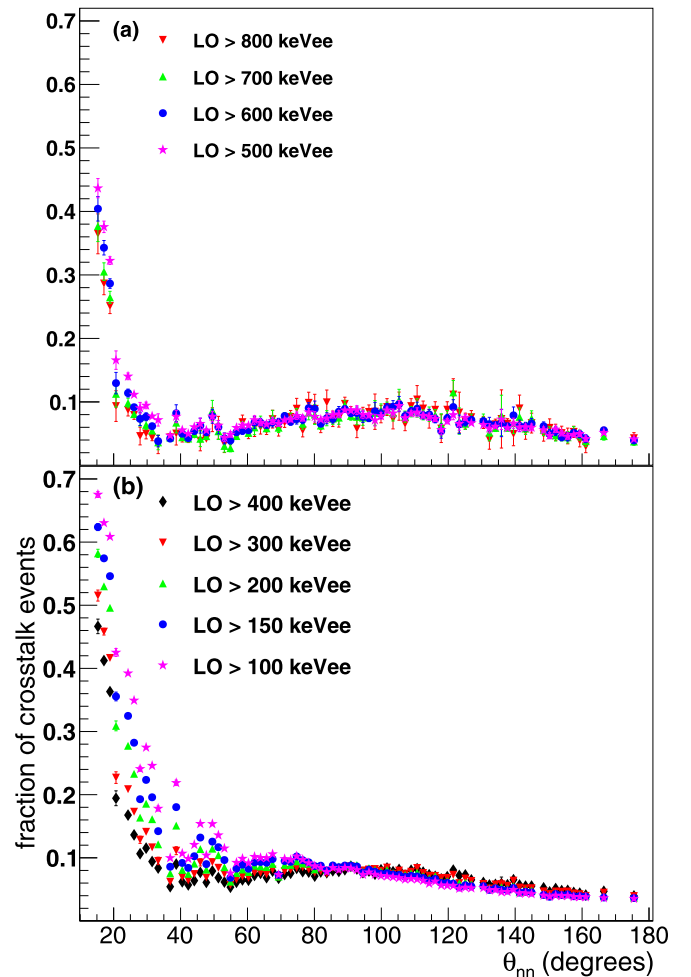


FIG. 13. Fraction of coincidences attributed to neutron cross talk as a function of the detector separation angle and for several light output thresholds.

In the remainder of the paper, multiple scattering corrections are applied to the neutron-neutron correlations. To obtain data corrected for cross talk, it suffices to correct each data point by the factors given in Fig. 13.

VI. COMPARISON OF THE DATA TO FREYA SIMULATIONS

Using a customized [44] version of MCNPX 2.7.0 with the LLNL Fission Library/FREYA [29,43,45] turned on, we simulated neutron-neutron angular correlations using the detector threshold to filter low energy neutrons, as done in previous analyses.

The first simulations are shown for the $^{252}\text{Cf}(\text{sf})$ source. The FREYA calculations are shown with open symbols in Fig. 15 while the full symbols are the data. The number of spontaneous fission events simulated was equivalent to 30 min of data taking. The energy-dependent experimental neutron detection efficiency was taken into account (see Fig. 4).

While the results do not match perfectly, FREYA qualitatively reproduces the experimental data. In particular, with the full detector simulation, the agreement with data is better than in Ref. [8] which concluded that there was no evidence for

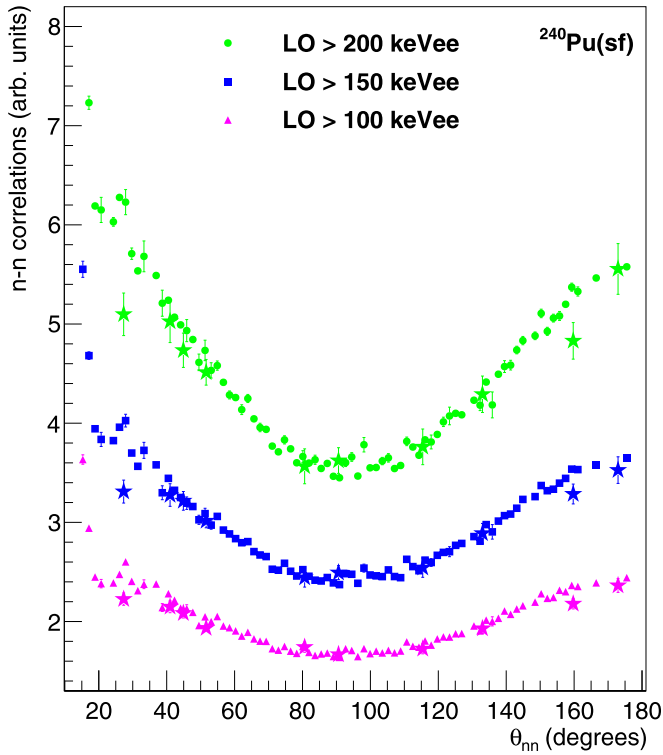


FIG. 14. The cross-talk and neutron acceptance corrected two-neutron angular correlation for $^{240}\text{Pu}(\text{sf})$ as a function of the angular separation and for several light output thresholds. The full circles, squares, and triangles are based on 23 h of data taking. The Marcath [6] measurements are shown with stars.

scission neutrons from the data. That conclusion is strengthened here with the most comprehensive $^{252}\text{Cf}(\text{sf})$ measurement to date.

Without FREYA turned on the distribution would be flat except for a peak at 0° due to neutron cross talk. For light output thresholds below 300 keVee and angles smaller than 25° , we observe deviations between measurements and simulations, likely due to the reasons stated in Sec. VC, i.e., insufficient model details in the simulation, etc. Table V lists the number of correlated neutron pairs for all detector pairs as a function of the light output threshold LO. The number of detected pairs for

TABLE V. Number of neutron pairs counted for all detector pairs, as a function of the light output threshold, for ^{252}Cf .

LO (keVee)	Neutron pairs
100	18 595 000
150	15 871 400
200	13 468 700
300	6 916 880
400	3 570 520
500	1 940 640
600	1 109 490
700	662 943
800	412 261

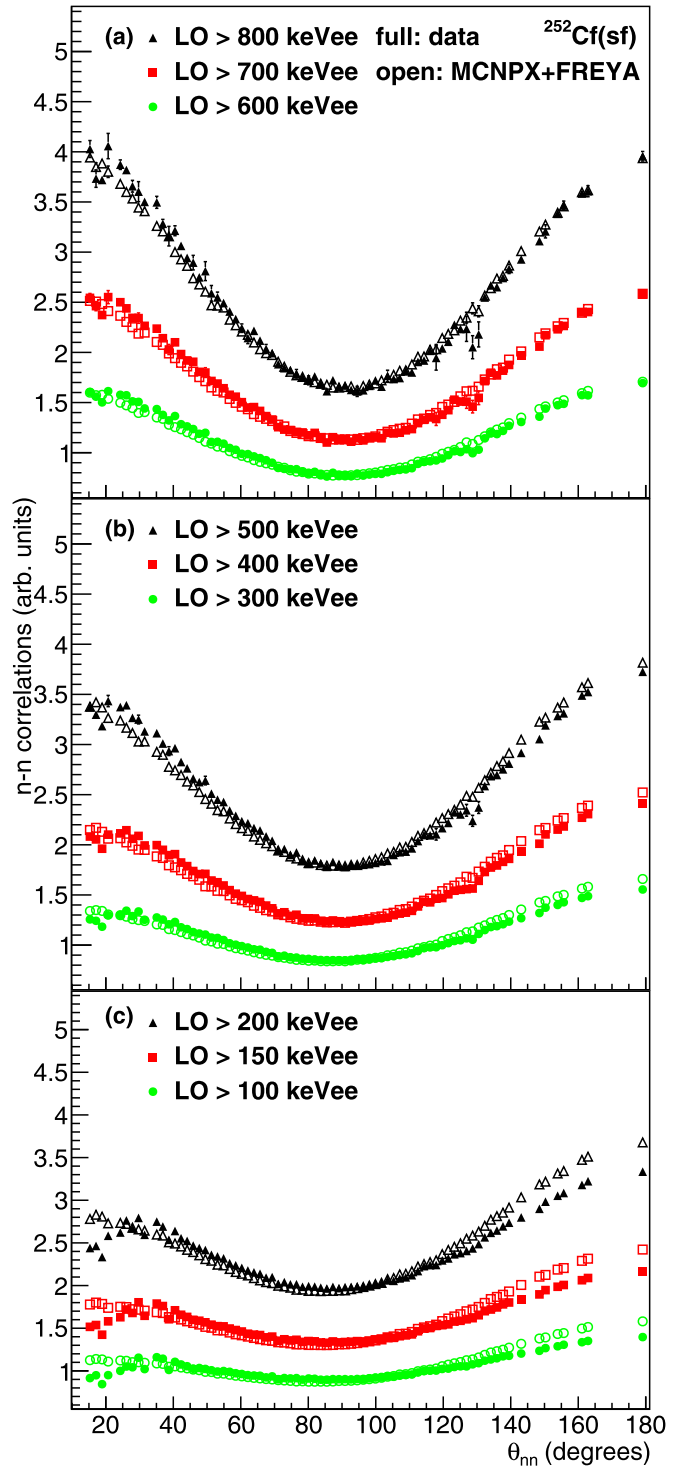


FIG. 15. The cross-talk and neutron acceptance corrected two-neutron angular correlation for $^{252}\text{Cf}(\text{sf})$ as a function of the angular separation and for several light output thresholds.

^{252}Cf is a factor of 9 greater than the number of detected pairs for ^{240}Pu (see Table IV), which explains the higher statistics.

FREYA includes several physics-motivated model parameters. In particular, the parameter x describes how the excitation energy is partitioned between the light, L , and heavy, H ,

fission fragments. If the two fragments are in mutual thermal equilibrium, equal temperature, $T_L = T_H$, the total excitation energy will, on average, be partitioned as $E_{\text{stat}} = \dot{E}_L^* + \dot{E}_H^*$ according to the heat capacities of the fragments. The heat capacities are assumed to be proportional to the corresponding Fermi-gas level density parameters a_L and a_H ,

$$\frac{\dot{E}_L^*}{\dot{E}_H^*} = \frac{a_L}{a_H}. \quad (6)$$

The observed neutron multiplicities suggest that the light fragment tends to be disproportionately excited [39]. Therefore, the average excitation energy is modified in favor of the light fragment,

$$\bar{E}_L^* = x \dot{E}_L^*, \bar{E}_H^* = E_{\text{stat}} - \bar{E}_L^*, \quad (7)$$

where the adjustable model parameter x is expected to be larger than unity.

The simulations for $^{252}\text{Cf}(\text{sf})$ were based on a “global” fit to a number of data sets: the Mannhart prompt fission neutron spectrum [48], prompt neutron multiplicity distribution [49], neutron multiplicity as a function of TKE [3], neutron multiplicity as a function of fragment mass [50], and average photon energy and multiplicity [51]. In particular, the neutron multiplicity as a function of fragment mass, $\nu(A)$, is sensitive to the x parameter. In this fit, $x = 1.27$ was found. This value of x means that the excitation energy of the light fragment is $\sim 30\%$ higher than that of the light fragment.

However, fewer data are available for $^{240}\text{Pu}(\text{sf})$ to fix the FREYA parameters. In particular, no $\nu(A)$ data are available to tune the x parameter for $^{240}\text{Pu}(\text{sf})$. Therefore, a default value of $x = 1.2$ was assumed previously since this was close to the value obtained for $^{239}\text{Pu}(n_{\text{th}},\text{f})$. The other FREYA parameters were either taken from the ^{252}Cf fit or tuned to the neutron multiplicity distribution and average neutron multiplicity. No global analysis has so far been done. Until such an analysis is complete, preferably with a larger number of observables included, some quantities, such as the average neutron energy, may not ultimately match reality. However, the calculations in Ref. [8], showed that the neutron-neutron angular correlations are sensitive to the value of x . Therefore, we can use our data to determine x for $^{240}\text{Pu}(\text{sf})$.

To determine the value of x that agrees best with our $^{240}\text{Pu}(\text{sf})$ data, we compare the data to four different x values between 1.1 and 1.4 in Fig. 16. The number of fissions simulated with FREYA was equivalent to the 23 h of data taking in the experiment. We see that increasing x effectively shifts and tilts the correlation from approximately equal intensity at 0° and 180° with $x = 1.1$ to a significantly higher correlation at 0° for $x = 1.4$. We note also that, in all cases, similarly for $^{252}\text{Cf}(\text{sf})$, increasing the strength of the correlation as the cutoff energy increases. Both behaviors can be explained by the characteristics of neutron evaporation.

The neutron-neutron correlation arises because, while the neutrons are emitted isotropically in the rest frame of the fragment, the boost to the laboratory frame means that the neutrons will preferentially follow the fragments. Thus, if one neutron is emitted from each fragment, they will be found at 180° apart while, if both are emitted from the same fragment,

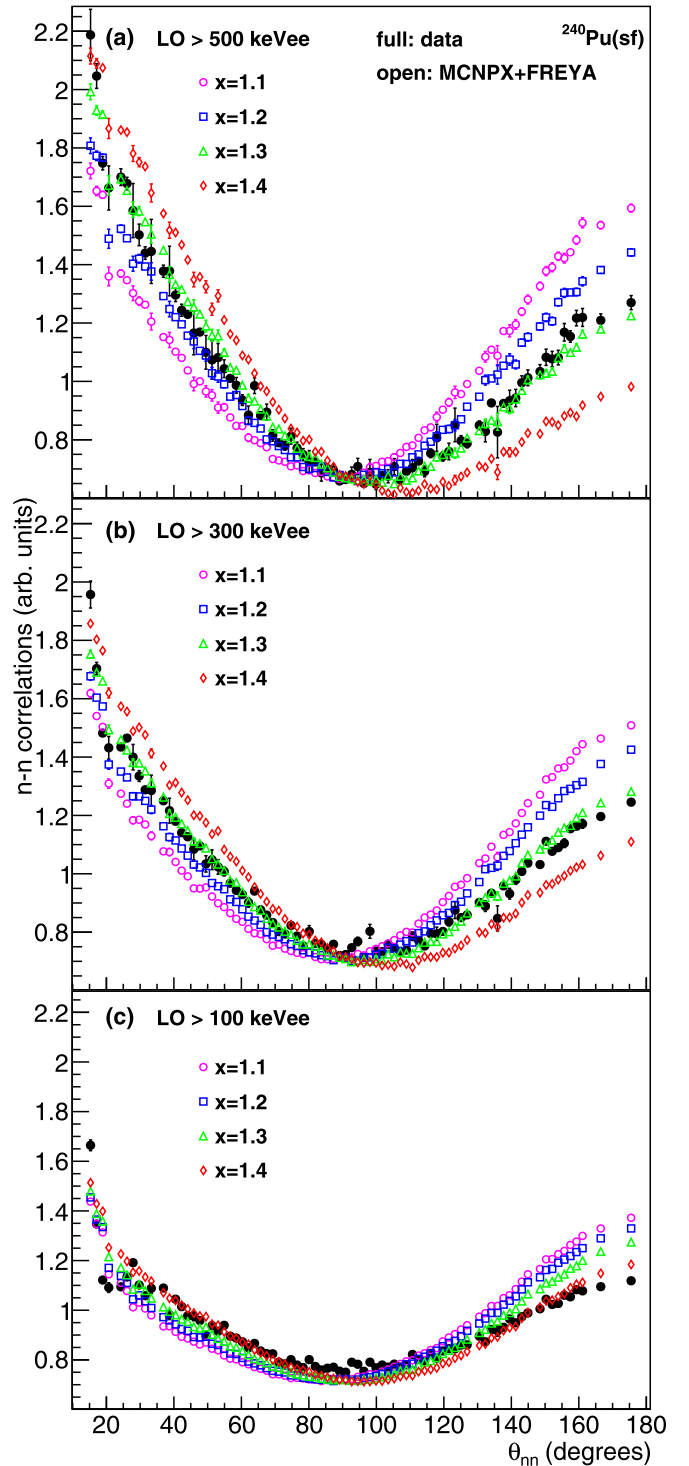


FIG. 16. The cross-talk and neutron acceptance corrected two-neutron angular correlation for $^{240}\text{Pu}(\text{sf})$ as a function of the angular separation and for several light output thresholds. FREYA calculations with $x = 1.1, 1.2, 1.3,$ and 1.4 are also shown.

the angular separation is 0° . The 0° correlation includes two parts: both neutrons emitted from the light fragment and both emitted from the heavy fragment. Since the light fragment is higher velocity to conserve momentum, the correlation from

two-neutron emission from the light fragment at 0° is larger. The three contributions combine to give peaks at 0° and 180° with a dip at 90° .

The light fragment also emits neutrons with larger kinetic energy on average. Therefore, increasing x , which gives even more excitation energy to the light fragment while removing it from the heavy fragment, increases the correlation at 0° while decreasing it at 180° . Likewise, increasing the neutron energy threshold increases the average energy of the neutrons that remain to form the correlation. Thus, the higher the neutron energy threshold, the larger the bias toward emission from the light fragment and the higher the 0° correlation relative to the back-to-back correlation at 180° . In addition, the higher energy cutoff would preferentially select neutrons that were emitted in the direction of the boost rather than those opposite the boost direction which would enhance the correlation as the energy increases.

We note that there are qualitative differences in the $^{252}\text{Cf}(\text{sf})$ and $^{240}\text{Pu}(\text{sf})$ correlations due to the different average neutron multiplicities as well. Since the average neutron multiplicity of $^{252}\text{Cf}(\text{sf})$ is ~ 3.76 , each fragment can emit more than one neutron and any two emitted neutrons can be used to form the correlation function. On the other hand, the average neutron multiplicity of $^{240}\text{Pu}(\text{sf})$ is ~ 2.1 so that, on average, the neutron-neutron correlation is formed from the only neutrons emitted during the fission. In addition, the average neutron energy of neutrons emitted from $^{252}\text{Cf}(\text{sf})$ is higher than those from $^{240}\text{Pu}(\text{sf})$ so that increasing the energy threshold is more likely to result in two peaks of equal strength for $^{252}\text{Cf}(\text{sf})$ than for $^{240}\text{Pu}(\text{sf})$. These characteristics can be observed in both the simulations and the data. The curves in Figs. 15 and 16, as well as Fig. 18, can be compared to the angular correlations obtained by running the standalone FREYA code. Those are shown for $^{252}\text{Cf}(\text{sf})$ and $^{240}\text{Pu}(\text{sf})$ in Fig. 17. With increasing kinetic energy thresholds, we observe that the peak at 0° rises whereas the peak at 180° decreases. This is more noticeable for $^{240}\text{Pu}(\text{sf})$ than for $^{252}\text{Cf}(\text{sf})$ due to the former's lower neutron multiplicity, as discussed above. FREYA is thus consistent with the above observations.

An examination of the results in Fig. 16 shows that $x = 1.3$ gives the optimal value compared to the $^{240}\text{Pu}(\text{sf})$ angular correlation data. This x value is quite close to the one determined from the global fit to $^{252}\text{Cf}(\text{sf})$. Figure 18 shows the comparison of our $^{240}\text{Pu}(\text{sf})$ data to FREYA calculations with $x = 1.3$. The agreement of the model calculations with the data after adjustment of x is quite good. The quality of the comparison of the simulations and the data again leave no room for a scission neutron contribution for this nucleus. Table IV lists the number of correlated neutron pairs for all detector pairs as a function of the light output threshold LO.

We have adjusted x to the measured $^{240}\text{Pu}(\text{sf})$ neutron-neutron angular correlation data assuming it is single-valued, an assumption common to all isotopes in FREYA. However, comparison with $^{252}\text{Cf}(\text{sf})$ data on the neutron multiplicity as a function of fragment mass suggests that x should be mass dependent. Modeling x as a function of fragment mass may improve the overall comparison of the angular correlation data with the simulations.

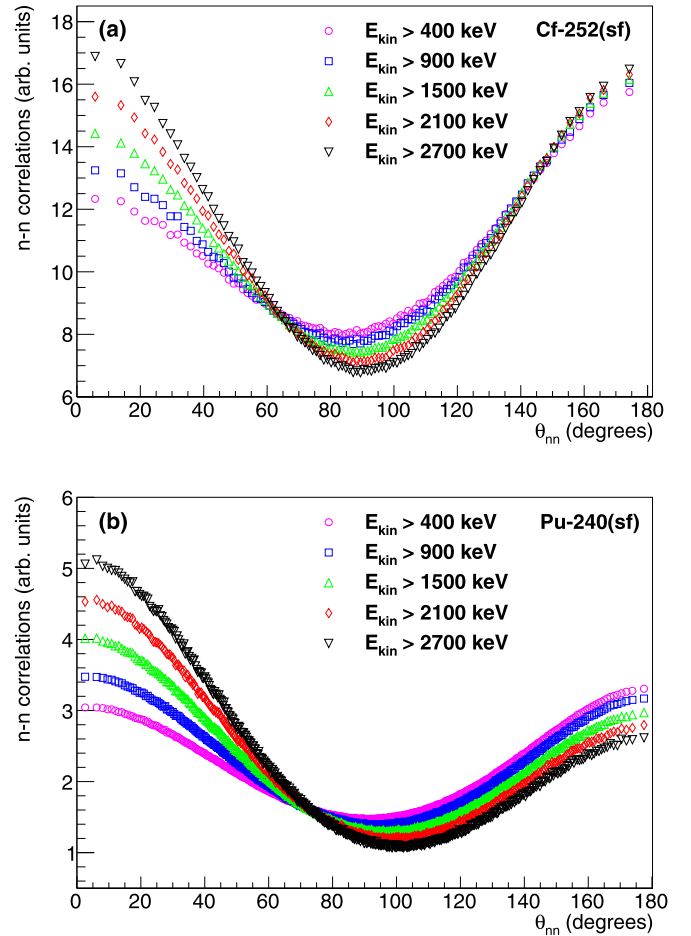


FIG. 17. The two-neutron angular correlation for $^{252}\text{Cf}(\text{sf})$ and $^{240}\text{Pu}(\text{sf})$ as a function of the angular separation, for several neutron kinetic energies. These curves were obtained by running FREYA in standalone mode, without transporting the neutrons and photons to the detectors. A value of $x = 1.3$ was used for $^{240}\text{Pu}(\text{sf})$.

VII. USING TIME-OF-FLIGHT CUTOFF TO FILTER NEUTRONS

In Secs. III A and V B, we pointed out the disadvantages of using a detector threshold to measure neutron-neutron correlations. This method of filtering out low energy neutrons is detector dependent, which impedes direct comparisons between measurements taken using different detectors. In this section, we analyze the correlations using time-of-flight to determine the neutron kinetic energy. This method, described in Sec. III B, to filter neutrons below a kinetic energy threshold is truly detector independent.

In the Monte Carlo simulations shown below, we account for the energy-dependent experimental neutron acceptance shown in Fig. 19. For low light output, the neutron acceptances are larger than in Fig. 4. Indeed, to determine particle type, events are now classified by combining not only PSD but also time-of-flight, so that the neutron identification region (magenta or light gray outline) in Fig. 3 can be broadened: a detection is identified as a neutron based on the time since the last photon

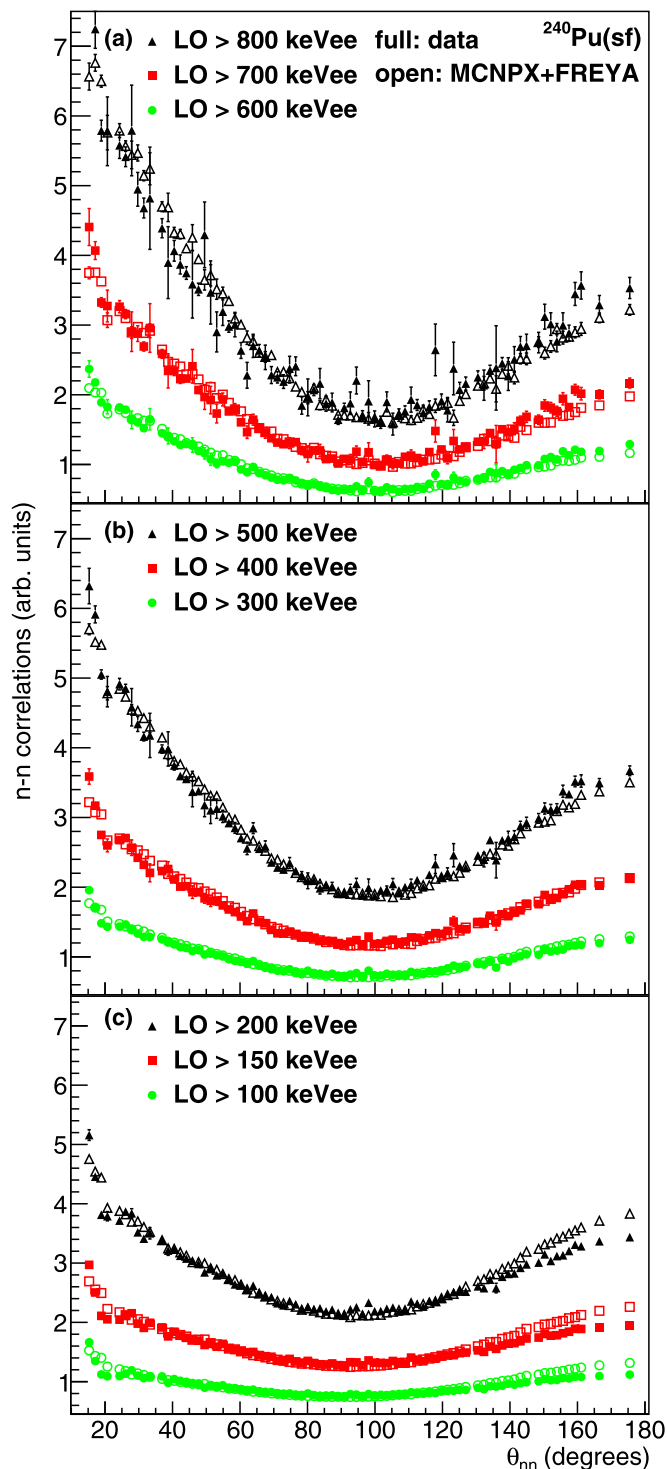


FIG. 18. The cross-talk and neutron acceptance corrected two-neutron angular correlation for $^{240}\text{Pu}(\text{sf})$ as a function of the angular separation and for several light output thresholds. Simulations with $x = 1.3$ are shown, see Eq. (7).

was detected and on whether it falls within the positive neutron identification region. Because of the larger positive neutron identification region, the fraction of detections classified as neutrons also rises.

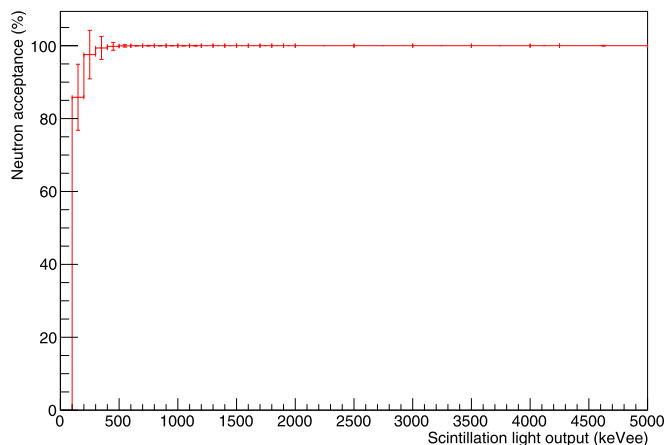


FIG. 19. Acceptance of neutron pulses as a function of scintillation light output and averaged over all detector channels. Bars indicate the dispersions around the means, from channel-to-channel variations.

Analyzing the same $^{252}\text{Cf}(\text{sf})$ data, we obtain the angular correlation shown in Fig. 20. Table VI lists the number of correlated neutron pairs for all detector pairs as a function of the neutron kinetic energy E_{kin} . For angles smaller than 30° , the correlations obtained by simulations are properly corrected for neutron cross talk, which confirms the validity of the correction method. However, the distributions measured experimentally are not properly corrected, especially at lower neutron kinetic energies. This is likely because the model inadequately represents details of the experimental setup, as discussed earlier. Therefore, this angular region cannot be trusted until neutron cross talk can be better modeled.

The correlations in Fig. 20 can be directly compared to the ones in Fig. 17(a) calculated using FREYA as a standalone code, i.e., without neutron transport to and through the detectors.

In Fig. 15, a detector threshold is imposed to set the minimum neutron kinetic energy required for detection. Most neutrons with the specified minimum neutron kinetic energy are, however, not recorded by the detector. Indeed, only those with the rare head-on collisions on hydrogen will produce a proton recoil with enough energy to produce sufficient scintillation light to be detected. For neutrons with twice the specified minimum neutron kinetic energy, only half of them will generate enough light to be counted. In Fig. 20 on the other hand, time-of-flight is used to determine the neutron kinetic energy, and many more neutrons close to the specified kinetic energy will thus be detected.

Higher energy neutrons are more strongly correlated than lower energy neutrons. Because the average energy of the neutron population measured by the detector threshold method is higher than that measured by the time-of-flight method, we expect to observe a stronger correlation employing a detector threshold.

Figure 21 directly compares the two methods to filter neutrons. The correspondence between the detector threshold LO and the neutron kinetic energy E_{kin} was taken from Eq. (2). The detector threshold neutron filter produces the curves with the open symbols and the curves with the full symbols result

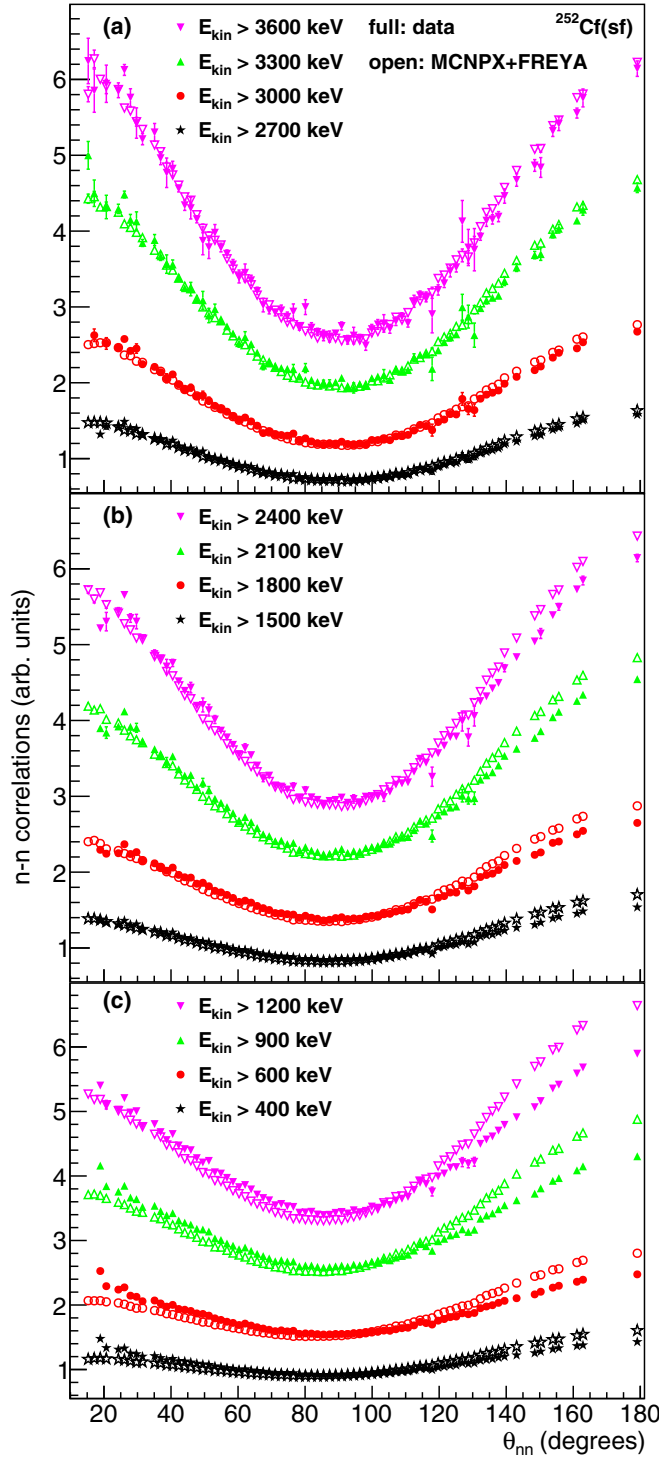


FIG. 20. The cross-talk and neutron acceptance corrected two-neutron angular correlation for $^{252}\text{Cf}(\text{sf})$ as a function of the angular separation, for several neutron kinetic energies. The neutron kinetic energy is determined from the neutron time-of-flight using a spontaneous fission photon trigger. FREYA simulations are also shown for the same kinetic energies.

from the data processed with the time-of-flight neutron filter. The former curves exhibit greater curvatures than the latter ones, confirming that the detector threshold method filters out

TABLE VI. Number of neutron pairs counted for all detector pairs, as a function of the neutron kinetic energy E_{kin} , for ^{252}Cf .

E_{kin} (keV)	Neutron pairs
400	5 354 740
600	4 968 180
900	4 460 580
1200	3 775 790
1500	2 928 350
1800	2 134 600
2100	1 506 130
2400	1 047 350
2700	726 013
3000	503 140
3300	349 751
3600	244 999

more low energy neutrons to produce a neutron population of higher average energy.

In Figs. 15 and 20, we observe that FREYA agrees well with both ways of filtering neutrons. The agreement with the experimental data is better than in Ref. [8] where FREYA was used as a standalone code. This is because FREYA is embedded in a radiation transport code that accounts for neutron kinematics effects within the detectors, whereas a standalone calculation ignores them.

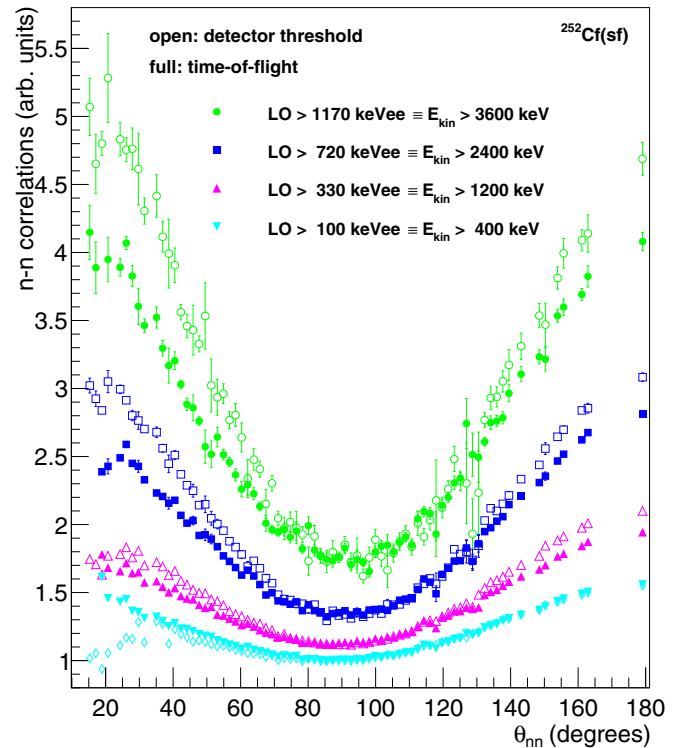


FIG. 21. The cross-talk and neutron acceptance corrected two-neutron angular correlation for $^{252}\text{Cf}(\text{sf})$ as a function of the angular separation, using either light output threshold (LO) or time-of-flight (E_{kin}) as a neutron filter.

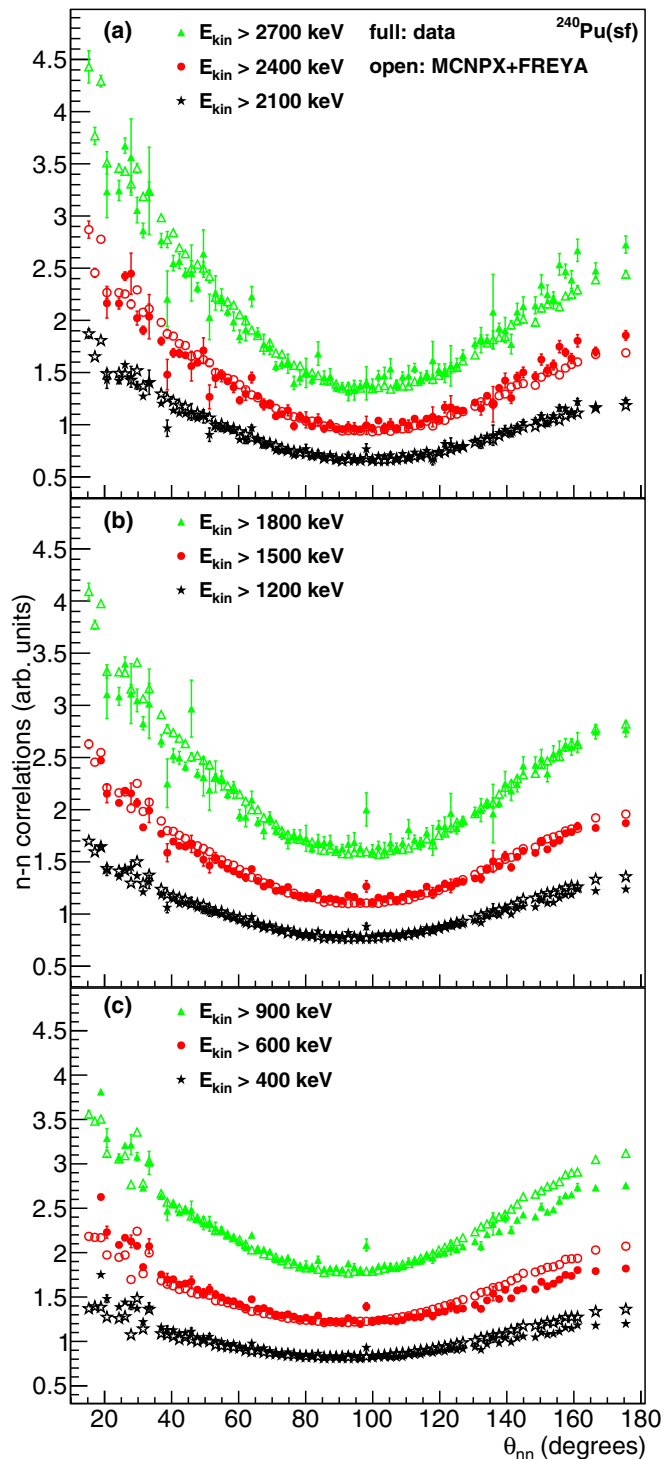


FIG. 22. The cross-talk and neutron acceptance corrected two-neutron angular correlation for $^{240}\text{Pu}(\text{sf})$ as a function of the angular separation. The neutron kinetic energy is determined from the neutron time-of-flight using a spontaneous fission photon trigger. FREYA simulations are also shown for the same kinetic energies.

The $^{240}\text{Pu}(\text{sf})$ data was analyzed using the same time-of-flight method. The results are shown in Fig. 22. Table VII lists the number of correlated neutron pairs for all detector pairs

TABLE VII. Number of neutron pairs counted for all detector pairs, as a function of the neutron kinetic energy E_{kin} , for ^{240}Pu .

E_{kin} (keV)	Neutron pairs
400	639 191
600	605 160
900	555 991
1200	469 720
1500	357 802
1800	254 164
2100	174 199
2400	117 258
2700	78 218

as a function of the neutron kinetic energy E_{kin} . Because of the low neutron yield of the source, the angular distributions above a neutron kinetic energy 2700 keV were not statistically significant. The most scintillation light a 2700 keV neutron can produce is about 828 keVee, which lies above the top distributions in Fig. 18. The correlations in Fig. 22 can be directly compared to those in Fig. 17(b) calculated using FREYA as a standalone code, i.e., without modeling the detector response using MCNPX.

VIII. CONCLUSIONS

We have measured the angular distributions of correlated neutrons emitted by spontaneous fission of ^{252}Cf and ^{240}Pu . To validate our experimental results, our $^{252}\text{Cf}(\text{sf})$ and $^{240}\text{Pu}(\text{sf})$ measurements were compared to previous measurements [4–6]. The agreement is overall reasonable. Differences can be attributed to the measurement method, which imposes a threshold on the scintillation light pulse to reject events. We show that this method depends on the detectors geometry and scintillation materials. We propose a second method to measure the neutron-neutron angular distributions based on time-of-flight. This method has the advantage of being detector independent. Angular distributions of correlated neutrons are shown using this time-of-flight approach for both isotopes.

To correct the neutron-neutron angular distributions from neutrons scattering multiple times between scintillators, a neutron cross-talk correction is also presented.

The event-by-event fission generator FREYA, together with the LLNL Fission Library, has been integrated into the Monte Carlo codes MCNP6.2 and MCNPX2.7.0. The combination of a physics-based fission event generator and an established radiation transport code leads to new capabilities: the simulation of correlations that conventional neutron Monte Carlo codes cannot predict. Using these codes, we were able to reproduce the experimentally measured distributions.

The asymmetry in the measured neutron-neutron angular distributions can be predicted by FREYA. The shape of the correlation function depends on how the excitation energy is partitioned between the two fission fragments. Experimental data suggest that the lighter fragment is disproportionately excited. The measured asymmetry enabled us to adjust the FREYA parameter x in ^{240}Pu , which controls the energy

partition between the fragments and is so far inaccessible in other measurements. In addition, the good agreement between the FREYA simulations and the high quality data of our analysis suggests a negligible contribution from scission neutrons, in agreement with the conclusions of Ref. [8].

Recent advances in scintillating materials have improved discrimination between neutrons and photons for low scintillation light outputs.

In the future, the authors plan on using these materials to better capture the full spectra of $^{252}\text{Cf}(\text{sf})$ and $^{240}\text{Pu}(\text{sf})$.

ACKNOWLEDGMENTS

This work was performed under the auspices of the U.S. Department of Energy by Lawrence Livermore National Laboratory under Contract No. DE-AC52-07NA27344. The authors acknowledge the Office of Defense Nuclear Nonproliferation Research and Development in DOE/NNSA for their support. J. Verbeke thanks his colleague A. Glenn for exchanging ideas and giving him comments based on his long experience in this area.

-
- [1] H. R. Bowman, S. G. Thompson, J. C. Milton, and W. J. Swiatecki, Velocity and angular distributions of prompt neutrons from spontaneous fission of ^{252}Cf , *Phys. Rev.* **126**, 2120 (1962).
- [2] J. S. Pringle and F. D. Brooks, Angular Correlation of Neutrons from Spontaneous Fission of ^{252}Cf , *Phys. Rev. Lett.* **35**, 1563 (1975).
- [3] C. Budtz-Jørgensen and H.-H. Knitter, Simultaneous investigation of fission fragments and neutrons in ^{252}Cf (sf), *Nucl. Phys. A* **490**, 307 (1988).
- [4] A. M. Gagarski, I. S. Guseva, V. E. Sokolov, G. V. Val'ski, G. A. Petrov, D. O. Krinitsin, D. V. Nikolaev, T. A. Zavarukhina, and V. I. Petrovaal, Neutron-neutron angular correlations in spontaneous fission of ^{252}Cf , *Bull. Russ. Acad. Sci.: Phys.* **72**, 773 (2008).
- [5] S. A. Pozzi, B. Wieger, A. Enqvist, S. Clarke, M. Flaska, M. Marcat, E. Larsen, R. C. Haight, and E. Padovani, Correlated neutron emissions from ^{252}Cf , *Nucl. Sci. Eng.* **178**, 250 (2014).
- [6] M. J. Marcat, T. H. Shin, S. D. Clarke, P. Peerani, and S. A. Pozzi, Neutron angular distribution in plutonium-240 spontaneous fission, *Nucl. Instrum. Meth. A* **830**, 163 (2016).
- [7] C. B. Franklyn, C. Hofmeyer, and D. W. Mingay, Angular correlation of neutrons from thermal-neutron fission of ^{235}U , *Phys. Lett. B* **78**, 564 (1978).
- [8] R. Vogt and J. Randrup, Neutron angular correlations in spontaneous and neutron-induced fission, *Phys. Rev. C* **90**, 064623 (2014).
- [9] Eljen technology, <http://www.eljentechnology.com>.
- [10] J. M. Verbeke, A. M. Glenn, G. J. Keefer, and R. E. Wurtz, Method for measuring multiple scattering corrections between liquid scintillators, *Nucl. Instrum. Methods A* **825**, 69 (2016).
- [11] J. M. Verbeke, *Calibration of Liquid Scintillators: I. Energy Calibration*, Tech. Rep. LLNL-TR-639553 (Lawrence Livermore National Laboratory, Livermore, CA, 2012).
- [12] J. M. Verbeke, M. K. Prasad, and N. J. Snyderman, Neutron crosstalk between liquid scintillators, *Nucl. Instrum. Methods A* **794**, 127 (2015).
- [13] J. M. Verbeke and S. A. Ouedraogo, *Calibration of Liquid Scintillators: II. Event Classifier using Pulse Shape Discrimination*, Tech. Rep. LLNL-TR-612312 (Lawrence Livermore National Laboratory, Livermore, CA, 2015).
- [14] J. M. Verbeke and S. A. Ouedraogo, *Calibration of Liquid Scintillators: III. Clock Synchronization between Scintillator Cells*, Tech. Rep. LLNL-TR-731500 (Lawrence Livermore National Laboratory, Livermore, CA, 2017).
- [15] R. A. Cecil, B. D. Anderson, and R. Madey, Improved predictions of neutron detection efficiency for hydrocarbon scintillators from 1 Mev to about 300 Mev, *Nucl. Instrum. Methods* **161**, 439 (1979).
- [16] J. M. Verbeke, A. M. Glenn, G. J. Keefer, and R. E. Wurtz, *Measurement of Quench Functions for Liquid Scintillators*, Tech. Rep. LLNL-TR-644625 (Lawrence Livermore National Laboratory, Livermore, CA, 2013).
- [17] W. Hansen and D. Richter, Determination of light output function and angle dependent correction for a stilbene crystal scintillation neutron spectrometer, *Nucl. Instrum. Methods A* **476**, 195 (2002).
- [18] Private communication with A. Glenn. Dr. Glenn devised a method to determine light output functions from measured pulse height distributions and individual proton recoil information recorded in Monte Carlo simulation (2016).
- [19] N. V. Kornilov, I. Fabry, S. Oberstedt, and F.-J. Hamsch, Total characterization of neutron detectors with a ^{252}Cf source and a new light output determination, *Nucl. Instrum. Methods A* **599**, 226 (2009).
- [20] A. Enqvist, C. C. Lawrence, B. M. Wieger, S. A. Pozzi, and T. N. Massey, Neutron light output response and resolution functions in EJ-309 liquid scintillation detectors, *Nucl. Instrum. Methods A* **715**, 79 (2013).
- [21] T. Goorley, Initial MCNP 6 release overview, *Nucl. Tech.* **180**, 298 (2012).
- [22] TRIPOLI-4 Project Team, TRIPOLI-4 version 8 User Guide, Tech. Rep. CEA-R-6316 (Commissariat à l'Énergie atomique et aux Énergies Alternatives, 2013).
- [23] TRIPOLI 4 Project Team, TRIPOLI-4, CEA, EDF and AREVA reference Monte Carlo code, *Ann. Nucl. Energy* **82**, 151 (2015).
- [24] D. E. Cullen, TART2005: *A Coupled Neutron-Photon 3-D, Combinatorial Geometry, Time Dependent Monte Carlo Transport Code*, Tech. Rep. UCRL-SM-218009 (Lawrence Livermore National Laboratory, Livermore, CA, 2005).
- [25] R. M. Buck and E. M. Lent, *COG User's Manual: A Multiparticle Monte Carlo Transport Code*, Tech. Rep. UCRL-TM-202590 (Lawrence Livermore National Laboratory, Livermore, CA, 2002).
- [26] T. E. Valentine, *MCNP-DSP Users Manual*, Tech. Rep. ORNL/TM-13334 R2 (Oak Ridge National Laboratory, Oak Ridge, Tennessee, 2001).
- [27] S. A. Pozzi, E. Padovani, and M. Marseguerra, MCNP-PoliMi: A Monte Carlo code for correlation measurements, *Nucl. Instrum. Methods A* **513**, 550 (2003).
- [28] E. Padovani, S. A. Pozzi, S. D. Clarke, and E. C. Miller, *MCNPX-PoliMi User's Manual*, Tech. Rep. C00791 MNYCP, Radiation Safety Information Computational Center (Oak Ridge National Laboratory, Oak Ridge, Tennessee, 2012).
- [29] J. M. Verbeke, C. Haggmann, and D. Wright, *Simulation of Neutron and Gamma Ray Emission from Fission and Photofission*. LLNL Fission Library 2.0.2, Tech. Rep. UCRL-

- AR-228518-REV-1 (Lawrence Livermore National Laboratory, Livermore, CA, 2016).
- [30] D. B. Pelowitz, J. W. Durkee, J. S. Elson, M. L. Fensin, J. S. Hendrichs, M. R. James, R. C. Johns, G. McKinney, S. G. Mashnik, J. M. Verbeke, L. S. Waters, and T. A. Wilcox, *MCNPX 2.7.0 Extensions*, Tech. Rep. LA-UR-11-02295 (Los Alamos National Laboratory, Los Alamos, NM, 2011).
- [31] Geant 4, <http://geant4.cern.ch>.
- [32] S. D. Clarke, E. C. Miller, M. Flaska, R. B. Pozzi, S. A. Oberer, and L. G. Chiang, Verification and validation of the `mcnp-x-polimi` code for simulations of neutron multiplicity counting systems, *Nucl. Instrum. Methods A* **700**, 135 (2013).
- [33] J. M. Verbeke, A. Dougan, L. F. Nakae, K. E. Sale, and N. J. Snyderman, Neutron correlations in special nuclear materials, experiments and simulations, *Proceedings of the 48th Annual INMM Conference and UCRL-PROC-231582* (Lawrence Livermore National Laboratory, 2007).
- [34] J. M. Verbeke, L. Nakae, P. Kerr, D. Dietrich, and A. Dougan, *Testing of Liquid Scintillator Materials for Gamma and Neutron Detection*, Tech. Rep. LLNL-CONF-414602 and Proceedings of the 50th Annual INMM Conference (Lawrence Livermore National Laboratory, 2009).
- [35] S. Lemaire, P. Talou, T. Kawano, M. B. Chadwick, and D. G. Madland, Monte Carlo approach to sequential neutron emission from fission fragments, *Phys. Rev. C* **72**, 024601 (2005).
- [36] S. Lemaire, P. Talou, T. Kawano, M. B. Chadwick, and D. G. Madland, Monte Carlo approach to sequential γ -ray emission from fission fragments, *Phys. Rev. C* **73**, 014602 (2006).
- [37] J. Randrup and R. Vogt, Calculation of fission observables through event-by-event simulation, *Phys. Rev. C* **80**, 024601 (2009).
- [38] R. Vogt, J. Randrup, J. Pruet, and W. Younes, Event-by-event study of prompt neutrons from $^{239}\text{Pu}(n,f)$, *Phys. Rev. C* **80**, 044611 (2009).
- [39] R. Vogt and J. Randrup, Event-by-event study of neutron observables in spontaneous and thermal fission, *Phys. Rev. C* **84**, 044621 (2011).
- [40] R. Vogt, J. Randrup, D. A. Brown, M. A. Descalle, and W. E. Ormand, Event-by-event evaluation of the prompt fission neutron spectrum from $^{239}\text{Pu}(n,f)$, *Phys. Rev. C* **85**, 024608 (2012).
- [41] R. Vogt and J. Randrup, Event-by-event study of photon observables in spontaneous and thermal fission, *Phys. Rev. C* **87**, 044602 (2013).
- [42] J. Randrup and R. Vogt, Refined treatment of angular momentum in the event-by-event fission model `freya`, *Phys. Rev. C* **89**, 044601 (2014).
- [43] J. M. Verbeke, J. Randrup, and R. Vogt, Fission reaction yield algorithm FREYA 2.0.2 user manual, *Comput. Phys. Commun.* **222**, 263 (2018).
- [44] J. M. Verbeke, *Customized MCNPX to Generate "List-Mode" ^3He Neutron Captures and Scintillator Counts*, Tech. Rep. LLNL-TM-671194 (Lawrence Livermore National Laboratory, Livermore, CA, 2015).
- [45] J. M. Verbeke, J. Randrup, and R. Vogt, Fission reaction yield algorithm `freya` for event-by-event simulation of fission, *Comput. Phys. Commun.* **191**, 178 (2015).
- [46] J. M. Verbeke, C. Haggmann, J. Randrup, and R. Vogt, *Integration of FREYA into MCNP6: An Improved Fission Chain Modeling Capability*, Tech. Rep. LLNL-PROC-638986 (Lawrence Livermore National Laboratory, Livermore, CA, 2013).
- [47] J. M. Verbeke, C. A. Haggmann, J. Randrup, and R. Vogt, Integration of `freya` and into `mcnp6`: An improved fission chain modeling capability, Proceedings of the 56th Annual INMM Conference, Vol. 2, 1291 (2015).
- [48] W. Mannhart, Properties of neutron sources, Proc. Advisory Group Mtg. Neutron Sources, Leningrad, USSR, June 1986, and IAEA-TECDOC-410, Vienna (1987).
- [49] J. W. Boldeman and M. G. Hines, Prompt Neutron Emission Probabilities Following Spontaneous and Thermal Neutron Fission, *Nucl. Sci. Eng.* **91**, 114 (1985).
- [50] V. N. Dushin, F.-J. Hamsch, V. A. Jakovlev, V. A. Kalinin, I. S. Kraev, A. B. Laptev, D. V. Nikolaev, B. F. Petrov, G. A. Petrov, V. I. Petrova, Y. S. Pleva, O. A. Shcherbakov, V. I. Shpakov, V. E. Sokolov, A. S. Vorobyev, and T. A. Zavarukhina, Facility for neutron multiplicity measurements in fission, *Nucl. Instrum. Methods A* **516**, 539 (2004).
- [51] R. Billnert, F.-J. Hamsch, A. Oberstedt, and S. Oberstedt, New prompt spectral γ -ray data from the reaction $^{252}\text{Cf}(sf)$ and its implication on present evaluated nuclear data files, *Phys. Rev. C* **87**, 024601 (2013).